NASA TECHNICAL NOTE **NASA TN D-7768**

NASA TN D-7768

(NASA-TN-D-7768) A PARAMETRIC STUDY OF EFFECT OF FOREBODY SHAPE ON FLOW ANGULARITY AT MACH 8 (NASA) 48 p HC $3.75 CSCL 20D

N75-10008

Unclas
H1/02 53794

A PARAMETRIC STUDY OF EFFECT OF FOREBODY SHAPE ON FLOW ANGULARITY AT MACH 8

by Charles B. Johnson and Don C. Marcum, Jr.

Langley Research Center
Hampton, Va. 23665

NATIONAL AERONAUTICS AND SPACE ADMINISTRATION • WASHINGTON, D. C. • NOVEMBER 1974

1. Report No. NASA TN D-7768	2. Government Accession No.	3. Recipient's Catalog No.
4. Title and Subtitle A PARAMETRIC STUDY OF EFFECT OF FOREBODY SHAPE ON FLOW ANGULARITY AT MACH 8		5. Report Date November 1974
		6. Performing Organization Code
7. Author(s) Charles B. Johnson and Don C. Marcum, Jr.		8. Performing Organization Report No. L-9639
		10. Work Unit No. 760-66-01-02
9. Performing Organization Name and Address NASA Langley Research Center Hampton, Va. 23665		11. Contract or Grant No.
		13. Type of Report and Period Covered Technical Note
12. Sponsoring Agency Name and Address National Aeronautics and Space Administration Washington, D.C. 20546		14. Sponsoring Agency Code
15. Supplementary Notes		

16. Abstract

Flow angularity and static pressure measurements have been made on the lower surface of nine forebody models that simulate the bottom forward surface of a hypersonic aircraft. Measurements were made in an area of the forebody that represents the location of an inlet of a scramjet engine. Tests were conducted at a Mach number of 8 for free-stream unit Reynolds numbers per meter of 28×10^6 for angles of attack of 0°, 5°, and 10° and 22×10^6 for angles of attack of 15° and 20°. A parametric variation of the forebody surface investigated the effect of: (1) spanwise curvature, (2) longitudinal curvature, and (3) planform shape on both flow angularity and static pressure distribution. Results of each of the three parametric variations of geometry were compared to those for the same flat-delta forebody. Spanwise-curvature results showed that a concave shape and the flat delta had the lowest flow angularity and lowest rate of increase in flow angularity with angle of attack. Longitudinal-curvature results showed a convex surface to give the better flow at the higher angles of attack. The better of the two planform shapes tested was a convex elliptical shape. Limited flow-field calculations were made at angles of attack using a three-dimensional, method-of-characteristics program. In general, at all angles of attack there was agreement between data and theory. From this study it appears that the forebody shape that would give the best flow for a scramjet engine inlet would be a surface with a combination of: (1) concave spanwise curvature, (2) longitudinal expansion, and (3) an elliptical planform.

17. Key Words (Suggested by Author(s)) Flow angularity – forebody; Hypersonic aircraft; Scramjet	18. Distribution Statement Unclassified – Unlimited; STAR Category 12

19. Security Classif. (of this report)	20. Security Classif. (of this page)	21. No. of Pages	22. Price*
Unclassified	Unclassified	46	$3.25

*For sale by the National Technical Information Service, Springfield, Virginia 22151

A PARAMETRIC STUDY OF EFFECT OF FOREBODY SHAPE ON FLOW ANGULARITY AT MACH 8

By Charles B. Johnson and Don C. Marcum, Jr.
Langley Research Center

SUMMARY

Flow angularity and static pressure measurements have been made on the lower surface of nine forebody models that simulate the bottom forward surface of a hypersonic aircraft. Measurements were made in an area of the forebody that represents the location of an inlet of a scramjet engine. Tests were conducted at a Mach number of 8 for free-stream unit Reynolds numbers per meter of 28×10^6 for angles of attack of 0°, 5°, and 10° and 22×10^6 for angles of attack of 15° and 20°. A parametric variation of the forebody surface investigated the effect of: (1) spanwise curvature, (2) longitudinal curvature, and (3) planform shape on both flow angularity and static pressure distribution. Results of each of the three parametric variations of geometry were compared to those for the same flat-delta forebody. Spanwise-curvature results showed that a concave shape and the flat delta had the lowest flow angularity and lowest rate of increase in flow angularity with angle of attack. Longitudinal-curvature results showed a convex surface to give the better flow at the higher angles of attack. The better of the two planform shapes tested was a convex elliptical shape. Limited flow-field calculations were made at angles of attack using a three-dimensional, method-of-characteristics program. In general, at all angles of attack there was agreement between data and theory. From this study it appears that the forebody shape that would give the best flow for a scramjet engine inlet would be a surface with a combination of: (1) concave spanwise curvature, (2) longitudinal expansion, and (3) an elliptical planform.

INTRODUCTION

The concept of a hypersonic aircraft with airbreathing engines has been investigated both experimentally and analytically by a large number of investigators. Summaries of work in this area are given in references 1 to 10. These vehicles, operating at hypersonic speeds, require scramjet propulsion systems to provide efficient thrust levels. Integration of a scramjet engine and an airframe is a complex problem which encompasses such basic disciplines as aerodynamics, structures, systems analysis, propulsion, and heat transfer. A picture of a model of a hypersonic research aircraft is shown in figure 1 which illustrates a typical engine-airframe installation where the forebody surface upstream of the scramjet engine acts as a precompression surface for the flow entering the engine. In order to approach a maximum efficiency for a scramjet engine it is desirable to produce good precompression with the forebody while maintaining a minimum variation of local flow angle at the inlet with changes in angle of attack.

This paper will focus on the forebody flow field by investigating the flow angle at the lower surface of nine parametric models that represent the lower forebody surface, along a spanwise plane that represents the location of the engine inlet. Flow angle at the inlet is primarily a function of the angle of attack of the forebody and the shape of the forebody. Typical local angles of attack along the precompression forebody surface for a hypersonic transport (ref. 11) and a hypersonic research airplane (ref. 12) are 9° and 10°, respectively, for cruise conditions; however, for various maneuvers it is expected that the angle of attack could change as much as plus or minus 10°. It is the purpose of this report to present measured flow angles, static pressure distributions, and the resulting change of flow angle with angle of attack in the downstream portion of nine forebody geometries at a location on the lower surface of the forebody models that would represent the location of an inlet to a scramjet engine. Results of this study should aid in the design of a forebody shape which will minimize the flow angularity at the inlet of the scramjet engine.

Flow angles and static pressures were measured at four stations across the semispan of the nine forebody models. Tests were conducted at a Mach number of 8 at free-stream Reynolds numbers per meter of 28×10^{6} for angles of attack of 0°, 5°, and 10° and 22×10^{6} for angles of attack of 15° and 20°.

SYMBOLS

B	base width
M	Mach number
p	pressure
Δp	pressure difference of the wedge portion of the flow-angularity probe
$p_{t,3}$	total pressure measured on the blunt leading edge of the flow-angularity probe
R	radius
T	absolute temperature

V	velocity
x,y,z	distances in x-, y-, and z-directions (see figs. 10 and 11)
z_{max}	maximum outboard distance of the forebody surface in the z-plane
α	model angle of attack
γ	ratio of specific heats
δ	local flow angle at the probe mounted at the center line of the model relative to the direction of the free-stream flow
ψ	spanwise flow angle at probe location
$\bar{\psi}$	spanwise probe alinement angle relative to the center line of the calibration plate

Subscripts:

e	local conditions
t,1	total conditions in the facility stagnation camber
w	wall
∞	free stream

APPARATUS AND TEST PROCEDURES

Test Apparatus

The tests were conducted in the Langley Mach 8 variable-density hypersonic tunnel (see fig. 2) at a unit Reynolds number per meter of 28×10^6 for angles of attack of 0°, 5°, and 10° and 22×10^6 for angles of attack of 15° and 20°. A Mach number calibration of the facility can be found in reference 13 and a further description is given in reference 14.

Description of Models

Forebody models.- Nine forebody models used for flow-angularity measurements are shown in figures 3 to 11. The models were mounted inverted in the tunnel as illustrated in figure 12. The bottom surface of the forebody models (windward surface at a positive angle of attack) represents the forward portion of the bottom surface of a hypersonic aircraft. The flow angularity is measured 3.81 cm from the base of the model in an area where the inlet of a scramjet engine would be located. All the models are 50.8 cm long and have a maximum base width B of 12.474 cm with the exception of model 9 which has a maximum width of 11.420 cm. The base cross-section shape from which models 2 to 7 are derived is model 1 which is basically a flat-bottom delta wing configuration with a 14° included angle (83° sweep angle), as shown in figure 3. Models 2, 3, and 4 are modified from the base planform of model 1 by varying the spanwise curvature of the bottom surface of the model with convex circular arcs with radii R of 24.948, 18.712, and 12.474 cm as shown in figures 4, 5, and 6, respectively. This parametric variation in the spanwise convex curvature results in B/R ratios of 0, 0.5, 0.667, and 1.0 for models 1, 2, 3, and 4, respectively. Model 5, shown in figure 7, has concave spanwise curvature with a B/R ratio of -0.5 and base radius of 24.948 cm which is the reverse curvature of model 2. The bottom surfaces of models 1 to 5 (see figs. 3 to 7) are conical segments formed by the curvature of the base and the sharp apex of the model. The sides of models 1 to 5 are flat surfaces which are inclined at an angle of 63.27° and pass through the sharp apex point of the model. The angle of attack of models 1 to 5 is defined as the angle between the wind vector and the conical ray in the plane of symmetry on the bottom of the model. Models 6 and 7 have bottom surfaces which result in a longitudinal compression and expansion of the forebody flow field as shown in figures 8 and 9, repectively. Models 6 and 7 have no spanwise curvature, and have the same sweep angle, planform, and side angles as model 1 (fig. 3). The concave surface (compression) of model 6 is formed by a circular arc of 845.82-cm radius (see fig. 8). The angle of attack of model 6 (fig. 8) is defined as the angle between the wind vector and a line on the plane of symmetry tangent to the bottom surface at the apex of the model. Model 6 was designed to provide 3.44° of compression from the nose to the base of the model. The convex surface (expansion) of model 7 (fig. 9) is formed by a circular arc 574.04 cm in radius in the upstream portion of the model and a flat surface 12.70 cm long at the base of the model. The flow on the bottom surface is expanded through an angle of 3.81° from the tip of the model to the base. The angle of attack of model 7 is defined as the angle between the wind vector and the flat surface at the base of the model. Models 6 and 7 have the same planform and side angles as described for model 1. Model 8, shown in figure 10, has a flat bottom surface with a planform which has sides formed by portions of an elliptical surface. The angle of attack and side angles for model 8 are the same as those described for model 1. Model 9, shown in figures 11 and 12, is an early conical-flow concept designed by the method of reference 12 representing a portion of the forebody for the hypersonic research aircraft (see fig. 1). Conical-forebody flows typically represented by model 9 were analytically verified using an explicit finite-difference computer program described in references 15 and 16. These conical forebodies were designed to produce constant spanwise pressure distributions at the vehicle cruise angle of attack which put the forebody at a local angle of attack of approximately 10°. Conical surfaces are formed by rays passing through the base of the model and through the apex of the model. The angle of attack for model 9 is defined as the angle between the wind vector and the conical ray on the bottom of the model that lies in the plane of symmetry. In figures 3 to 11 there is a base view of the model showing the four positions of the flow-angularity probe. For each of these positions of the probe there is a static pressure orifice directly under the probe. The models in figures 3 to 11 were all constructed from 416 stainless steel.

Flow-angularity probe.- A drawing of the flow-angularity probe is shown in figure 13. The probe is mounted on the base of the model (see fig. 12) in four positions with an alinement relative to the model surface that puts the bottom surface of the probe parallel to the plane that is tangent to the model surface directly under the probe. In addition, the plane of symmetry of the probe is parallel to the center line of the model for the four probe positions at the base of the model. The flow-angularity probe is a blunt symmetrical wedge with a 30° included wedge angle. The blunt leading edge of the wedge has a pressure orifice centered on it which is used to measure the pitot pressure in the flow field. The flow angularity is determined from the difference in pressure in the two symmetrical orifices on the wedge portion of the probe.

Calibration plate for the flow-angularity probe.- In order to determine the flow angularity from the probe measurements on the nine forebody models, the probe was calibrated on a flat plate shown in figure 14. The probe was positioned at the base of a flat plate at angles relative to the flow over the plate of 0°, 2°, 4°, 6°, 8°, 10°, and 12° as indicated in figure 14. The probe alinement angle $\bar{\psi}$ was changed by installing a different adapter for each of the seven angular positions of the probe on the plate. The local Mach number upstream of the probe was varied by positioning the plate at angles of attack of 0°, 5°, 10°, 15°, and 20°.

Test Procedures

Test conditions.- The tests were conducted at a free-stream Mach number of 8 with free-stream total pressures of 10.4 MN/m^2 and 13.9 MN/m^2 and with a total temperature of approximately 800 K. The free-stream Reynolds number per meter was 28×10^6 for tests at angles of attack of 0°, 5°, and 10° and was 22×10^{6} for angles of attack of 15° and 20°. The $T_w/T_{t,1}$ ratio for the forebody models was approximately 0.5 for all tests.

Test methods and instrumentation.- The first phase of the test program consisted of a calibration of the flow-angularity probe using the calibration plate and the second phase consisted of measurement of the flow angularity and static pressure on the nine forebody models. Flow-angularity measurements were obtained during different test runs with the flow-angularity probe set at a given station and with the model set at the desired angle of attack prior to each run. Pitot pressure on the blunt leading edge of the flow-angularity probe was measured with a strain-gage transducer with a range of 0 to 0.345 kN/m^2. The pressure difference on the wedge portion of the probe was measured with a differential multirange capacitance-type transducer. Local surface pressures were obtained from four pressure orifices connected to multirange capacitance-type transducers. The electrical outputs from the transducers were recorded on magnetic tape and processed by an electronic data processing system.

Flow-Angularity Probe

The nine forebody models were tested at angles of attack of 0°, 5°, 10°, 15°, and 20° with the flow-angularity probe placed at four stations at the base of the model as indicated in figures 3 to 11. The position of the bow shock wave relative to the probe was determined for several models with a flow-field calculation using the three-dimensional, method-of-characteristics program of reference 15. The flow-field program of reference 15 is primarily designed to calculate slab delta-type bodies and continuously curved cross sections are restricted to ellipses which resulted in a rounding of the corner as illustrated by the solid line at the corners of the model in figure 15. The results of a typical calculation using the geometry generated by the program (solid line) rather than the actual model geometry (dashed line), made at angles of attack of 5° and 20° for model 9, are shown in figure 15 with the shock located at the upstream tip of the probe ($x = 47$ cm). At $\alpha = 5^{\circ}$ the shock is well above the probes. However, at $\alpha = 20^{\circ}$ the shock moves closer to the probe and for rounded-corner input geometry (solid line) there is an indication of possible probe-shock interference. If the actual geometry could have been calculated, it is believed that the predicted shock standoff distance would have been greater at the corners and would have cleared the probe in the outboard station.

Probe calibration.- The results of the flow-angularity-probe calibration are shown in figure 16 in terms of the measured probe parameter $\Delta p/p_{t,1}$ and the local Mach number. The probe was calibrated on a flat plate for values of $\bar{\psi}$ of 2°, 4°, 6°, 8°, 10°, and 12° (see fig. 14). The probe was also tested at $\bar{\psi} = 0^{\circ}$ in order to aline the probe in the flow with a zero flow-deflection reading. For each value of $\bar{\psi}$ the probe was calibrated with the plate set at angles of attack of 0°, 5°, 10°, 15°, and 20° resulting in measured local Mach numbers of 7.53, 6.87, 5.79, 4.76, and 3.86, respectively. The local Mach number was calculated from the static pressure p_e and from the pitot pressure measured with the probe $p_{t,3}$ using the following equation:

$$\frac{p_{t,3}}{p_e} = \left[\frac{(\gamma + 1)M_e^2}{2}\right]^{\frac{\gamma}{\gamma-1}} \left[\frac{(\gamma + 1)}{2\gamma M_e^2 - (\gamma - 1)}\right]^{\frac{1}{\gamma-1}} \tag{1}$$

The Mach number of 7.53 at $\alpha = 0^{\circ}$, determined with $p_{t,3}/p_e$ using equation (1), is attributed in part to the viscous interaction effects on the plate surface which are much more pronounced at zero angle of attack (ref. 17). The probe was calibrated for a given local Mach number and value of $\bar{\psi}$ in terms of the ratio of the pressure difference between the two sides of the wedge Δp and the total pressure in the settling chamber of the facility. For a given value of $\bar{\psi}$ the parameter $\Delta p/p_{t,1}$ increases as the local Mach number decreases, and in general has an increasing negative slope with increasing values of $\bar{\psi}$.

Forebody-flow-angle data reduction.- The measured flow angle of the nine forebody models was obtained with the measured values of $\Delta p/p_{t,1}$ and M_e using figure 16. Equation (1) is used to obtain the local Mach number M_e from the measured value of $p_{t,3}/p_e$. The local Mach number for both the calibration plate and for the nine forebody models is used only as a reference condition for obtaining ψ. In using equation (1) it was assumed that the static pressure on the surface of the model was approximately the same as the static pressure directly upstream of the probe. This assumption appeared to be justified from the results of flow-field calculations from a three-dimensional, method-of-characteristics program (ref. 18) which indicated the change in static pressure normal to the surface to be relatively small. Thus, once the local Mach number was determined, the flow angularity was obtained by interpolation on figure 16. The accuracy of the measurement of the flow angularity was determined to be $\pm 0.1^{\circ}$, based on the accuracy of the instrumentation and the accuracy of the model alinement in the flow.

RESULTS AND DISCUSSION

Forebody Flow-Field Models

Effect of spanwise curvature.- The results of flow-angularity measurements on forebody models 1, 2, 3, 4, 5, and 9 are shown in figure 17 for three spanwise locations.

These measurements were made to study the effect of spanwise curvature on the flow angularity. The angularity measurements were evaluated at stations of 30, 60, and 80 percent of the semispan at angles of attack of 5°, 10°, 15°, and 20°. Some flow-angularity measurements were evaluated at zero angle of attack but only for the 30 percent semispan location. Flow angularity at $\alpha = 0^{\circ}$ could not be measured at the 60 and 80 percent stations because the local Mach number exceeded 8 for these stations and a calibration (see fig. 16) could not be obtained for $M_e > 8$. The calibration could not be obtained because the calibration plate choked the tunnel flow when it was set at a negative angle of attack $\left(\text{i.e., an angle of attack that should give a } M_e > 8\right)$. In the actual flow-angularity measurements the probes were not always exactly at the 30, 60, and 80 percent semispan stations; therefore, the values shown in figure 17 had to be interpolated for the exact spanwise location. The distance used to determine the percent of semispan was measured in a plane perpendicular to the plane of symmetry (i.e., z-plane, see fig. 11). Models 1, 2, 3, 4, and 5 have the same planform and only the spanwise curvature of the models is varied. Model 9 has the same length as the other five, but has a slightly different base width. For the models in figure 17, the model angle of attack and the local flow angle at the model center line δ are the same; however, this is not true for model 6, therefore flow-angularity data for all models are plotted against the local flow angle. The data in figure 17 show a sharp increase in both the level of the flow angularity and in the slope $(d\psi/d\delta)$ as the semispan increases from 30 to 80 percent. A comparison of the results from models 1, 2, 3, and 4 indicates that at all three semispan stations, for all angles of attack, a $B/R = 1$ ratio (model 4) has, in general, the largest flow angularity and as B/R is decreased to zero (model 1) the flow angle and $d\psi/d\delta$ correspondingly decrease. The greatest value of flow angularity for the three semispan stations was found for either model 4 or model 9, which is expected because for model 4 $B/R = 1.0$ and for model 9 $B/R \approx 0.8$. It is interesting to note that for the 30 percent semispan station, model 9, which was a preliminary forebody design of a hypersonic research airplane, with $B/R \approx 0.8$, has a flow angularity which is much less than that for models 3 and 4 which have B/R ratios of 0.667 and 1.0, respectively. Model 5, which is the only model that has a concave spanwise surface, has the smallest flow angularity for all three semispan stations at local flow angles of 10°, 15°, and 20°. The greatest variation of flow angularity for a given angle of attack is found at the 60 and 80 percent stations at $\delta = 20^{\circ}$ where the highest and lowest values of ψ varied by an increment of approximately 2.2°.

Effect of longitudinal curvature.- Results of flow-angularity measurements made on forebody models with longitudinal convex curvature (expansion) and concave curvature (compression) surfaces (models 7 and 6) are shown in figure 18. Measurements were made for the same semispan stations and angles of attack as described for figure 17. However, for model 6 the angle of attack and the local flow angle δ at the probe differed; therefore, for a given model angle of attack the local angle of attack for model 6 is higher than the model angle of attack. The results of models 6 and 7 are compared to the results of model 1 which has a flat surface. The results show a trend similar to that found in figure 17 as the semispan station increases from 30 to 80 percent and as the local flow angle increases from 5° to 20° (i.e., flow angularity increases at each semispan location with increasing α). Figures 18(a) and 18(b) show nearly similar results for all three models both in the level of ψ and in the value of $d\psi/d\delta$. The results at the 80 percent semispan station for the compression surface (model 6) and the flat surface (model 1) are nearly identical; however, the expansion surface (model 7) shows a decrease in the level of ψ at $\delta = 15^{\circ}$, and significant reduction in $d\psi/d\delta$ from 5° to 15° local angle of attack.

Effect of planform.- Measurements of flow angularity (see fig. 19) were made on flat-bottom models of two different planform shapes – one a delta planform (model 1) and the other with an elliptical planform (model 8). The measurements were made for the same semispan stations and angles of attack as described in figures 17 and 18. For the models in figure 19 the model angle of attack and the local flow angle at the probe are the same. The results from the two models indicate that the elliptical planform of model 8 has a lower flow angle at the higher angles of attack. From angles of attack of 10° to 20° the value of $d\psi/d\delta$ for model 8 is less than that of model 1 at the 60 and 80 percent semispan stations.

Comparison of Data and Theory

Comparisons of the theoretical and experimental values of flow angularity, spanwise static pressures, and local Mach number for model 9 at angles of attack of 5°, 10°, 15°, and 20° are presented in figures 20, 21, and 22. The theoretical calculations were made with the three-dimensional, method-of-characteristics program described in reference 18. As was previously noted in figure 15, the geometry used in the computer program differed slightly from the actual geometry of the model in the area of the corner beyond a spanwise distance of approximately $z = 4.5$ cm. Because the model geometry used in the theoretical calculations was different from the actual model geometry, the theoretical calculations in figures 20, 21, and 22 are not shown beyond a spanwise distance of $z = 4.5$ cm. The data shown in these figures were taken on the center line ($z = 0$) and at stations which are approximately 1/3, 2/3, and 3/3 (see fig. 11) of the model semispan. The prediction of the flow angularity in figure 20 at the $z = 1.83$ cm station is in reasonably close agreement with data. At angles of attack greater than 5° for the spanwise locations the theory falls below the data. The theoretical surface static pressure distributions in figure 21 agree with the data but tend to underpredict slightly. It should be noted that the pressure distribution at the design angle of attack of 10° is constant in both theory and experiment. In figure 22 a comparison of the theoretical and experimental Mach number, evaluated at the probe position, shows that there is agreement between theory and data.

All of the model geometries (models 1 to 9) could not be represented adequately by the geometry methodology employed in the three-dimensional, method-of-characteristics program of reference 18. In addition, numerical difficulties occurred at several angles of attack which prohibited a continuous calculation from nose to the representative inlet station. Therefore, the characteristic calculations available for direct comparison are somewhat limited. Also, as stated previously, the numerical models differed significantly from the experimental models at spanwise locations greater than $z = 5$ cm; therefore, pressure data beyond this spanwise location are omitted from the comparisons for models 2, 3, 4, and 8.

Spanwise static pressure distributions measured at the four probe stations are shown in figure 23 for models 1 to 8. In general, the pressure distributions are nearly flat $\left(\frac{d\frac{p_e}{p_\infty}}{dz} \approx 0\right)$ for angles of attack of 0°, 5°, and 10° and the theory shows reasonable agreement with the data but tends to underpredict. At the outboard stations for models 2, 3, and 4 at $\alpha = 0^\circ$ the data indicate a decrease in pressure with increasing z for these models. The dropoff in the pressure data at zero angle of attack is believed due to a small outflow similar to that found in reference 19 for a delta wing at $\alpha = 0^\circ$. For angles of attack of 15° and 20° the increase in spanwise curvature from $B/R = 0$ to $B/R = 1.0$, for models 1 to 4 (figs. 23(a) to 23(d)), results in an increasing dropoff in static-pressure level at the outboard stations. The concave spanwise surface of model 5 (fig. 23(e)) produces a nearly constant pressure at all angles of attack. The longitudinal concave (compression) and convex (expansion) surfaces of models 6 and 7, respectively (figs. 23(f) and 23(g)), produce a nearly constant pressure at $\alpha = 15^\circ$ but show a slight decrease at the outboard station at $\alpha = 20^\circ$. The elliptical planform of model 8 (fig. 23(h)) showed a decrease in pressure at angles of attack of 15° and 20°.

CONCLUDING REMARKS

Flow-angularity measurements have been made near the base of nine forebody models that simulate that part of the bottom surface of a hypersonic aircraft that lies upstream of the inlet of a scramjet engine. Tests were made at a free-stream Mach number of 8 for a free-stream unit Reynolds number per meter of 28×10^6 for angles of attack of 0°, 5°, and 10°, and 22×10^6 for angles of attack of 15° and 20°. The nine forebody shapes were designed to investigate the effect of: (1) spanwise curvature, (2) longitudinal curvature, and (3) planform shape on flow angularity and spanwise pressure distribution. The results of the flow-angularity measurements for the three geometric effects were always compared to a basic flat-bottom delta configuration at 30, 60, and 80 percent of the semispan and are as follows:

(1) The spanwise-curvature study showed that the flat-bottom delta configuration had a smaller rate of change in flow angularity with a change in angle of attack than models with convex spanwise curvature. The model with concave spanwise curvature had the lowest rate of change in flow angularity with local flow angle of all models with spanwise curvature.

(2) The longitudinal-curvature study showed the longitudinal concave (compression) surface and flat-delta configuration had approximately the same rate of change in flow angularity with a change in local flow angle at all semispan stations. The longitudinal convex (expansion) surface had a lower rate of change in flow angularity with a change in local flow angle than the flat delta up to a local angle of attack of 15° for the 60 and 80 percent semispan stations.

(3) The planform study showed that the elliptical planform with a flat botton had approximately the same rate of change in flow angularity with angle of attack at 30 percent of the semispan as the flat-delta configuration. However, the rate of change in flow angularity with angle of attack for the elliptical planform decreased considerably at the two outboard semispan stations compared to the flat delta resulting in the lowest rate of change in flow angularity up to an angle of attack of 15° for all the models tested.

A comparison of the spanwise static pressure distribution at an angle of attack of 20° showed the spanwise concave surface to give the flattest distribution, while the other surfaces showed a decrease in pressure at the outboard station which was amplified with increasing convex curvature. In general the pressure distribution became flatter with decreasing angle of attack. For all angles of attack, several inviscid static pressure calculations showed agreement with the data, but tended to underpredict the data slightly.

Theoretical calculations of the flow angularity compared to the results from one model (model 9) indicate that at 5° angle of attack there is agreement between theory and data. However, with increasing angles of attack the theory falls below the measured flow angles.

The results of this study indicated that the forebody shape that would appear to give a nearly constant pressure level across the base and have the lowest change of flow angularity with angle of attack would be a surface with a combination of: (1) concave spanwise curvature, (2) longitudinal convex curvature, and (3) an elliptical planform.

Langley Research Center,
National Aeronautics and Space Administration,
Hampton, Va., September 5, 1974.

REFERENCES

1. Nagel, A. L.; and Becker, J. V.: Key Technology for Airbreathing Hypersonic Aircraft. AIAA Paper No. 73-58, Jan. 1973.

2. Becker, John V.; and Kirkham, Frank S.: Hypersonic Transports. Vehicle Technology for Civil Aviation – The Seventies and Beyond, NASA SP-292, 1971, pp. 429-445.

3. Becker, John V.: Prospects for Actively Cooled Hypersonic Transports. Astronaut. & Aeronaut., vol. 9, no. 8, Aug. 1971, pp. 32-39.

4. Kirkham, Frank S.; Cubbage, James M., Jr.; Vahl, Walter A.; and Small, William J.: Studies of Airframe-Propulsion-System Integration for Mach 6 Cruise Vehicles. NASA TN D-4128, 1967.

5. Gregory, Thomas J.; Williams, Louis J.; and Wilcox, Darrell E.: The Airbreathing Launch Vehicle for Earth Orbit Shuttle – Performance and Operation. J. Aircraft, vol. 8, no. 9, Sept. 1971, pp. 724-731.

6. Henry, J. R.; and McLellan, C. H.: Air-Breathing Launch Vehicle for Earth-Orbit Shuttle – New Technology and Development Approach. J. Aircraft, vol. 8, no. 5, May 1971, pp. 381-387.

7. Henry, John R.; and Beach, H. Lee: Hypersonic Air-Breathing Propulsion Systems. Vehicles Technology for Civil Aviation – The Seventies and Beyond, NASA SP-292, 1971, pp. 157-177.

8. Ferri, A.: Review of Scramjet Propulsion Technology. J. Aircraft, vol. 5, no. 1, Jan.-Feb. 1968, p. 3.

9. Johnston, P. J.; Cubbage, J. M.; and Weidner, J. P.: Studies of Engine-Airframe Integration on Hypersonic Aircraft. J. Aircraft, vol. 8, no. 7, July 1971, pp. 495-501.

10. Cubbage, James M.; and Kirkham, Frank S.: Investigation of Engine-Exhaust-Airframe Interference on a Cruise Vehicle at Mach 6. NASA TN D-6060, 1971.

11. Ellison, James C.: Investigation of the Aerodynamic Characteristics of a Hypersonic Transport Model at Mach Numbers to 6. NASA TN D-6191, 1971.

12. Edwards, C. L. W.: A Forebody Design Technique for Highly Integrated Bottom-Mounted Scramjets With Application to a Hypersonic Research Airplane. NASA TM X-71971, 1974.

13. Stainback, P. Calvin; Wagner, Richard D.; Owen, F. Kevin; and Horstman, Clifford C.: Experimental Studies of Hypersonic Boundary-Layer Transition and Effects of Wind-Tunnel Disturbances. NASA TN D-7453, 1974.

14. Schaefer, William T., Jr.: Characteristics of Major Active Wind Tunnels at the Langley Research Center. NASA TM X-1130, 1965.

15. Gunness, R. C., Jr.; Knight, C. J.; and D'Sylva, E.: Flow Field Analysis of Aircraft Configurations Using a Numerical Solution to the Three-Dimensional Unified Supersonic/Hypersonic Small-Disturbance Equations. Part I. NASA CR-1926, 1972.

16. D'Sylva, E.: Flow Field Analysis of Aircraft Configurations Using a Numerical Solution to the Three-Dimensional Unified Supersonic/Hypersonic Small-Disturbance Equations. Part II. NASA CR-1926, 1972.

17. Hayes, Wallace D.; and Probstien, Ronald F.: Hypersonic Flow Theory. Academic Press, Inc., 1959.

18. Chu, C. W.; and Powers, S. A.: The Calculation of Three-Dimensional Supersonic Flows Around Spherically-Capped Smooth Bodies and Wings. Volume I. Theory and Applications. AFFDL-TR-72-91, Vol. I, U.S. Air Force, Sept. 1972.

19. Bertram, Mitchel H.; Cary, Aubrey M., Jr.; and Whitehead, Allen H., Jr.: Experiments With Hypersonic Turbulent Boundary Layers on Flat Plates and Delta Wings. Hypersonic Boundary Layers and Flow Fields, AGARD CP No. 30, May 1968, pp. 1-1 to 1-21.

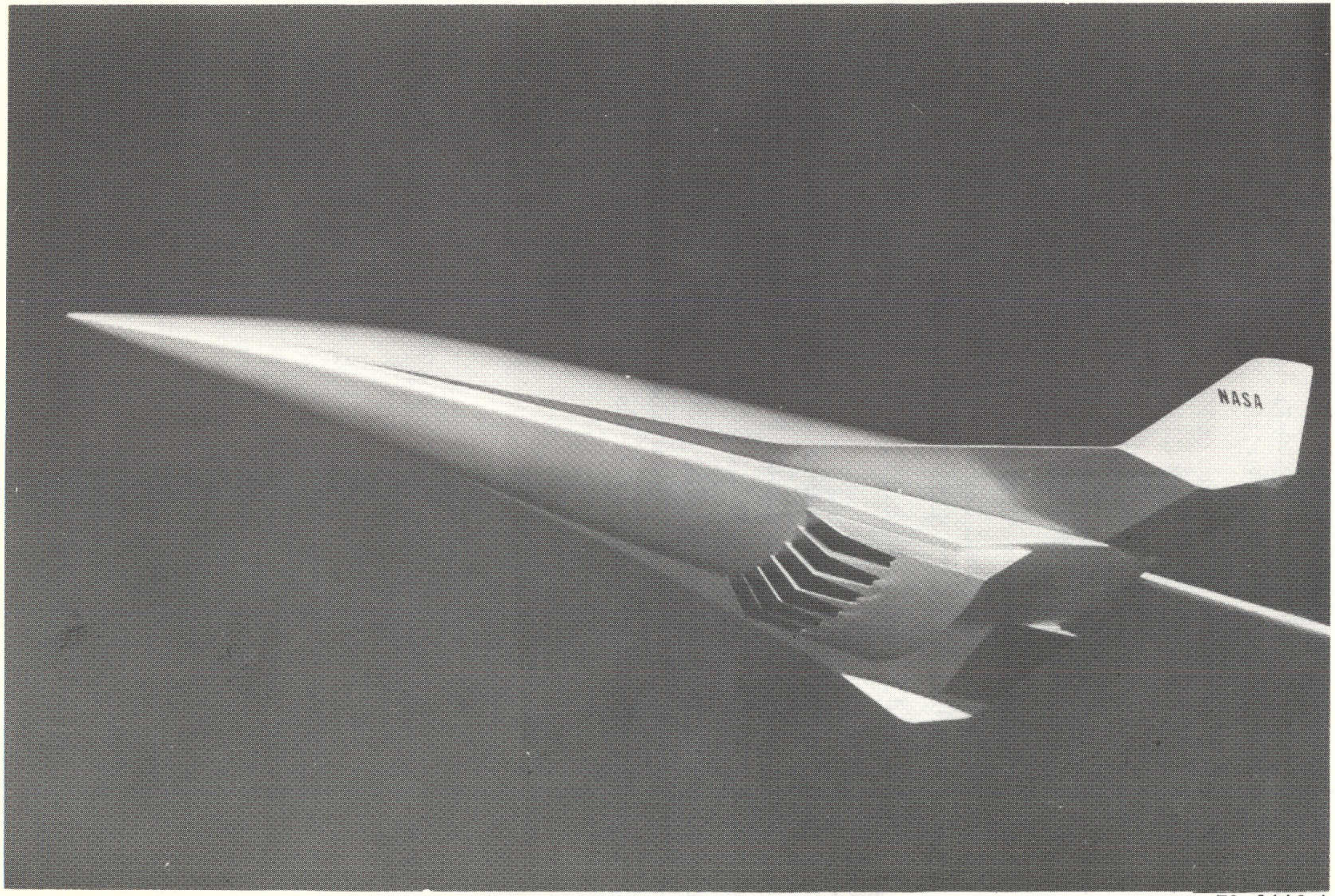

L-72-9146.1

Figure 1.- Model of a hypersonic research airplane.

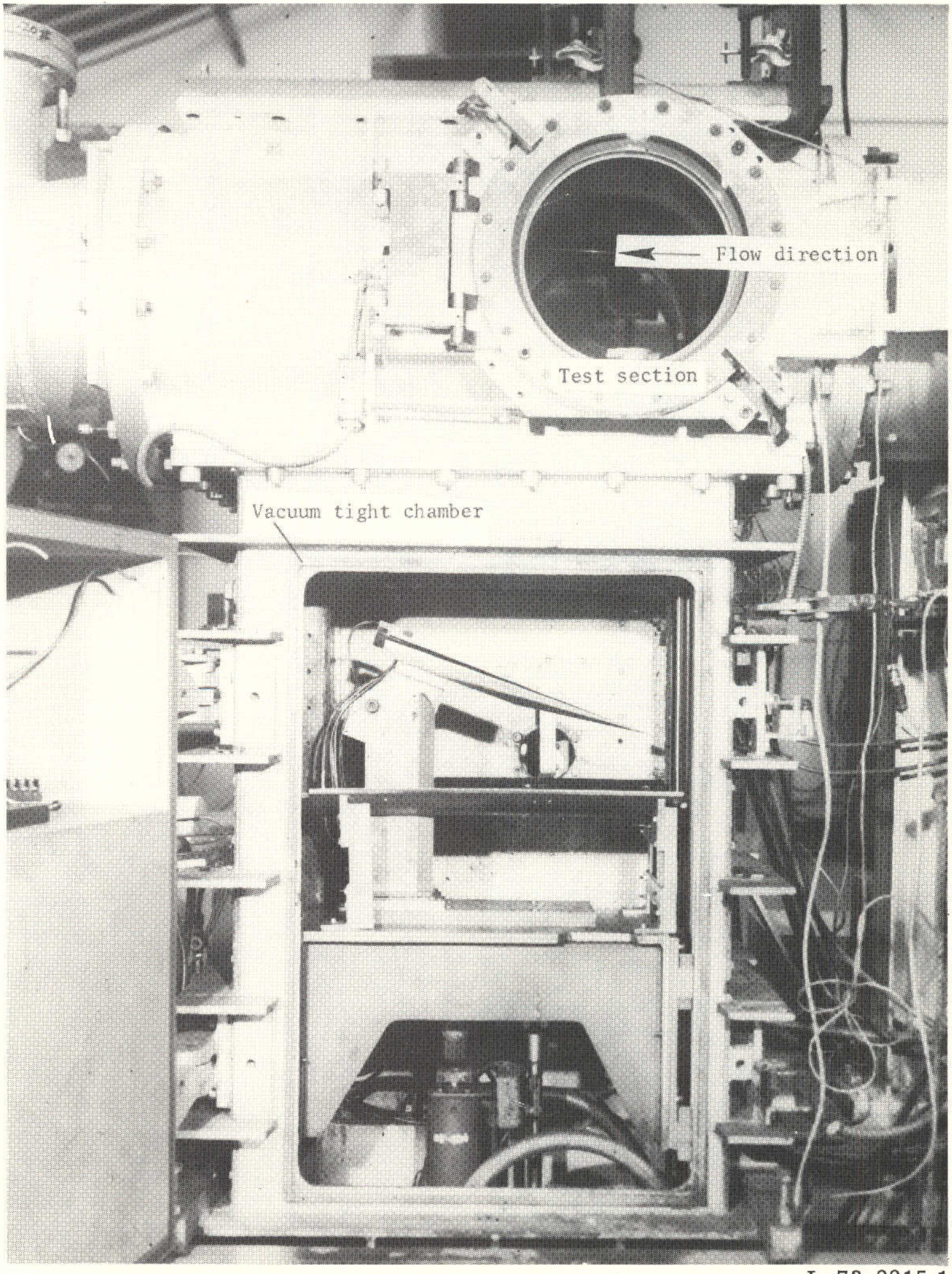

L-73-8815.1

Figure 2.- Mach 8 tunnel apparatus showing forebody model.

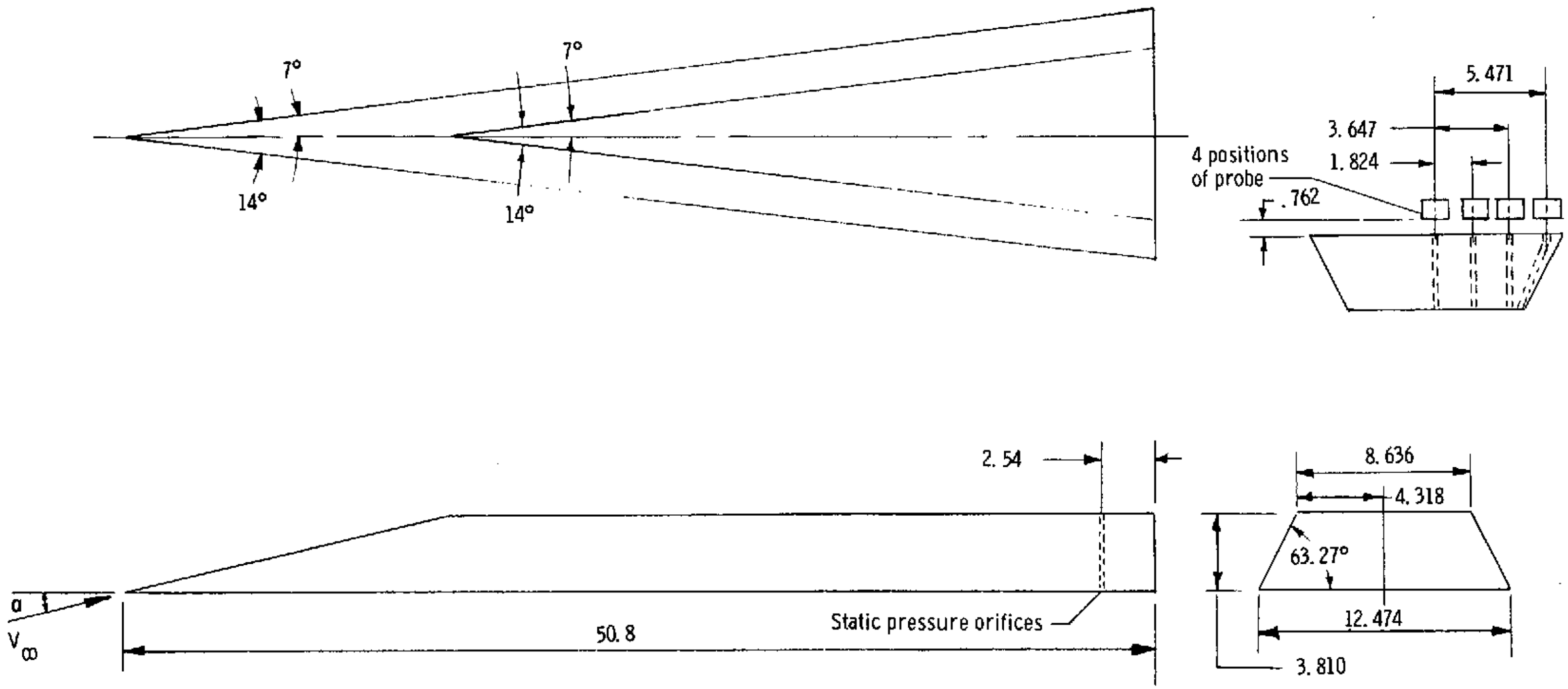

Figure 3.- Model number 1 – flat-delta planform (B/R = 0). All linear dimensions are in centimeters.

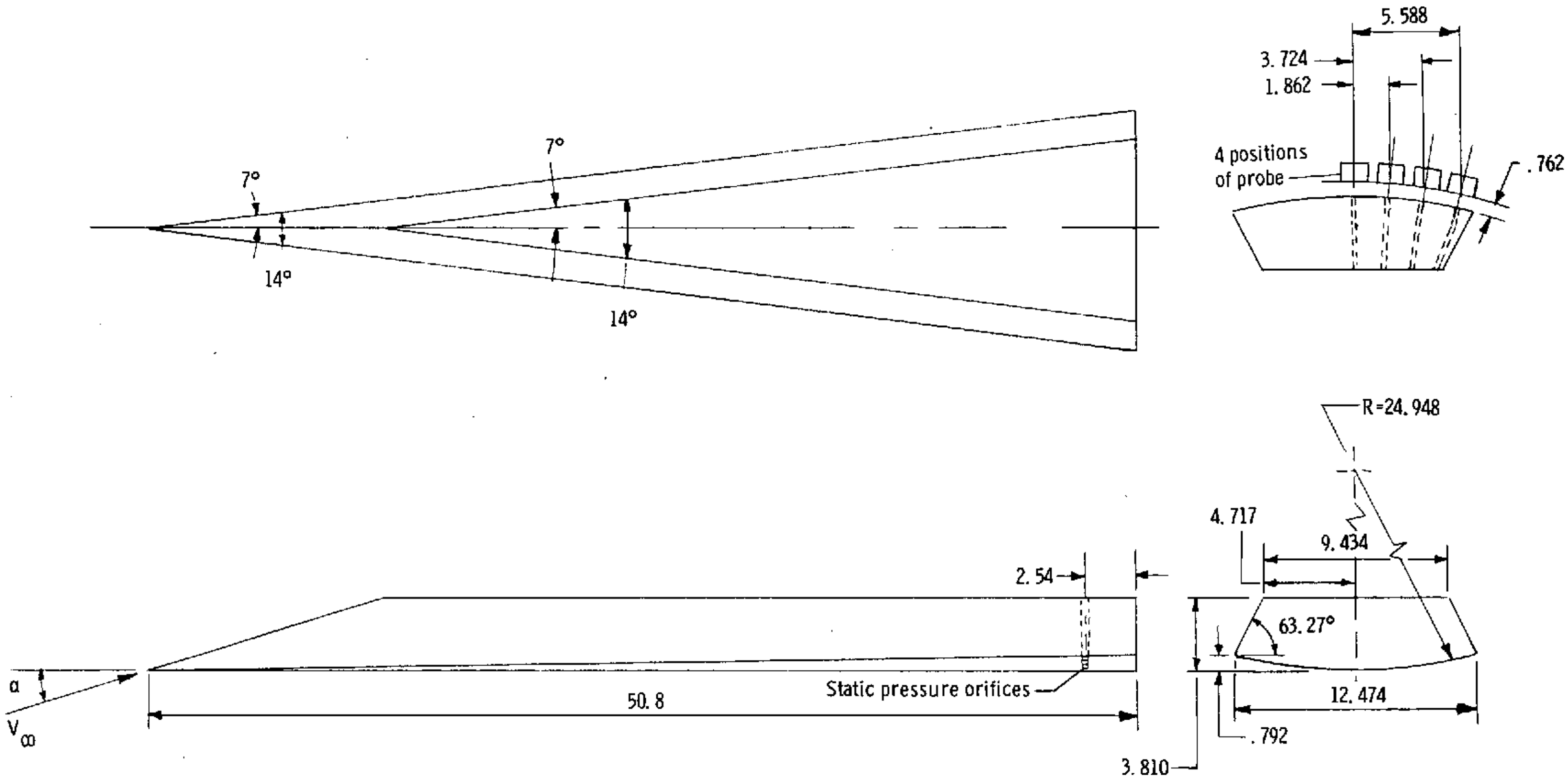

Figure 4.- Model number 2 – spanwise-convex surface (B/R = 0.5). All linear dimensions are in centimeters.

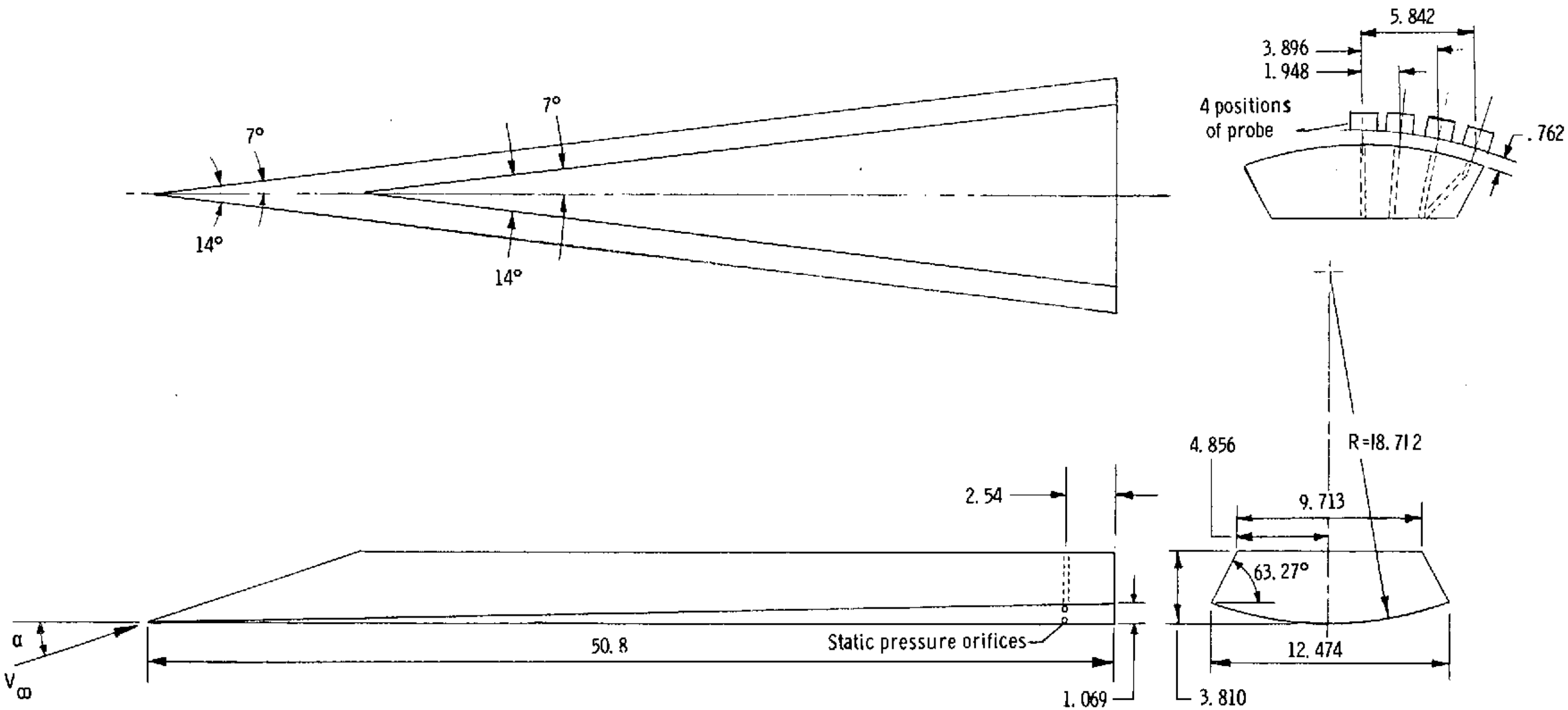

Figure 5.- Model number 3 – spanwise-convex surface (B/R = 0.667). All linear dimensions are in centimeters.

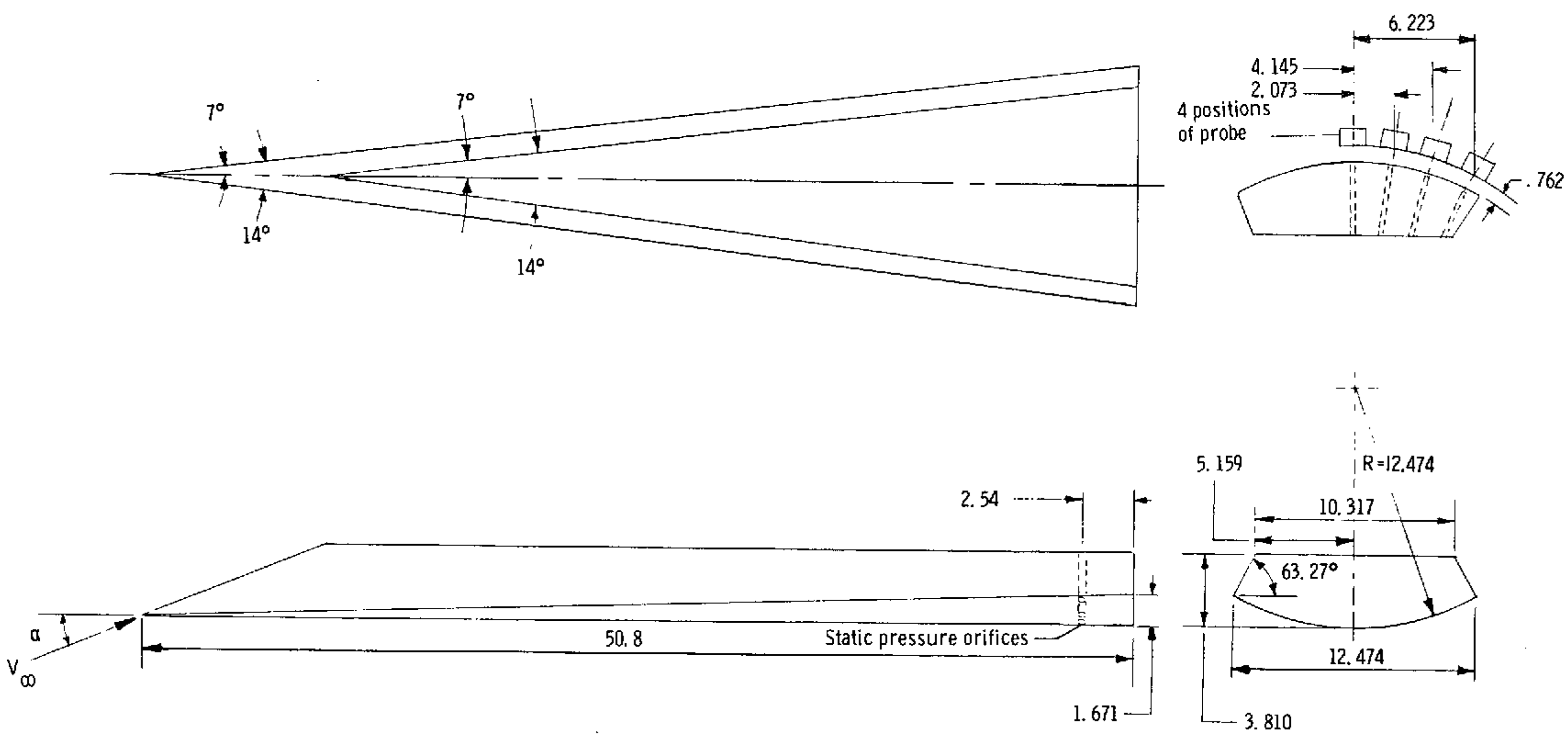

Figure 6.- Model number 4 – spanwise-convex surface (B/R = 1.0). All linear dimensions are in centimeters.

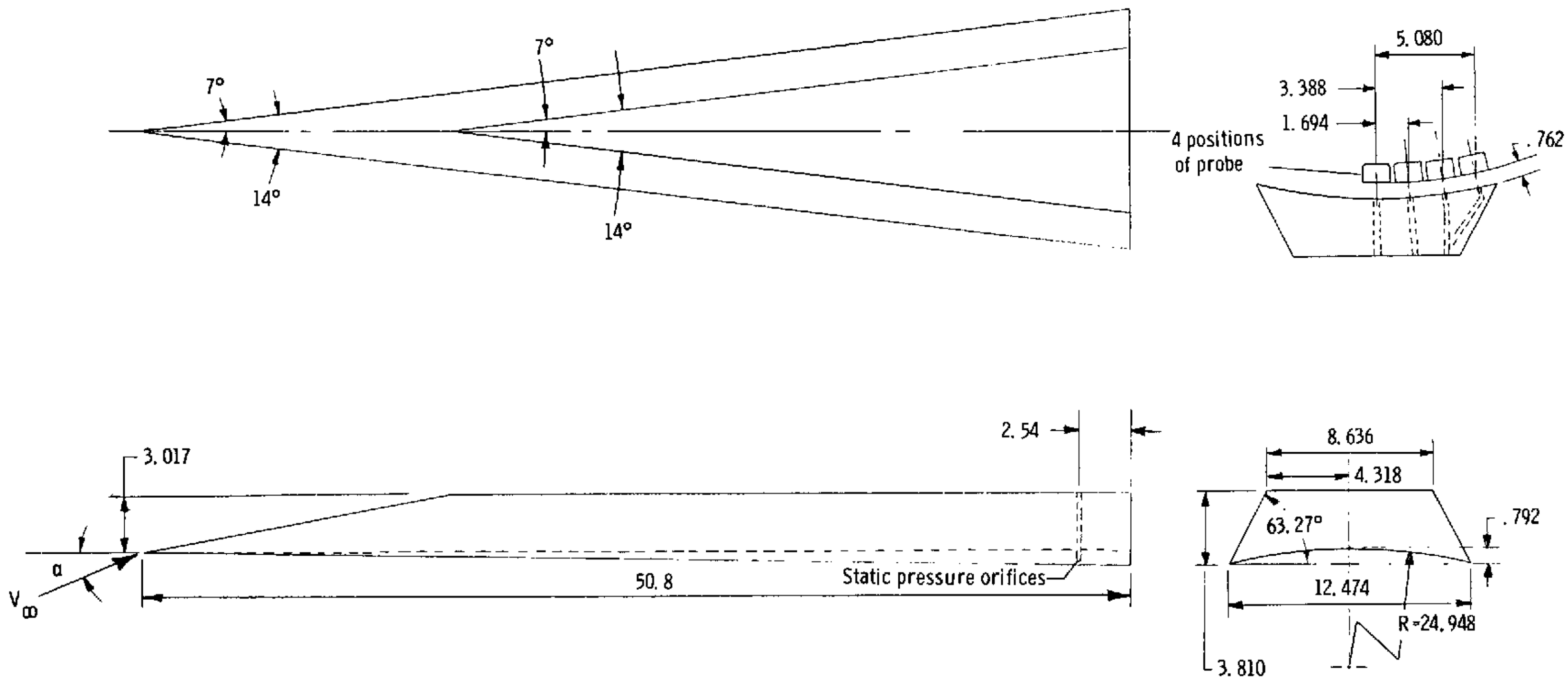

Figure 7.- Model number 5 – spanwise-concave surface (B/R = -0.5). All linear dimensions are in centimeters.

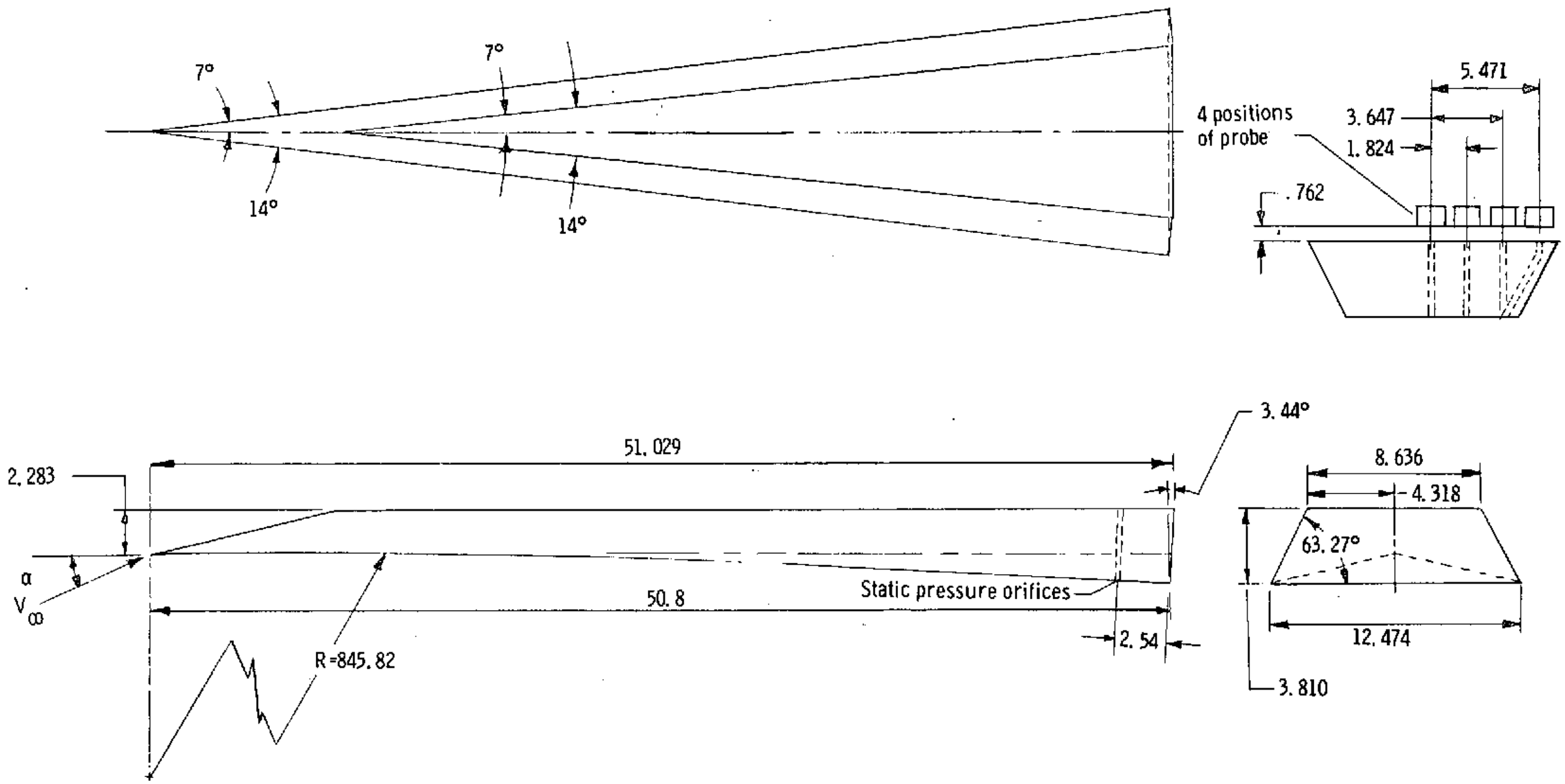

Figure 8.- Model number 6 – longitudinal-concave surface. All linear dimensions are in centimeters.

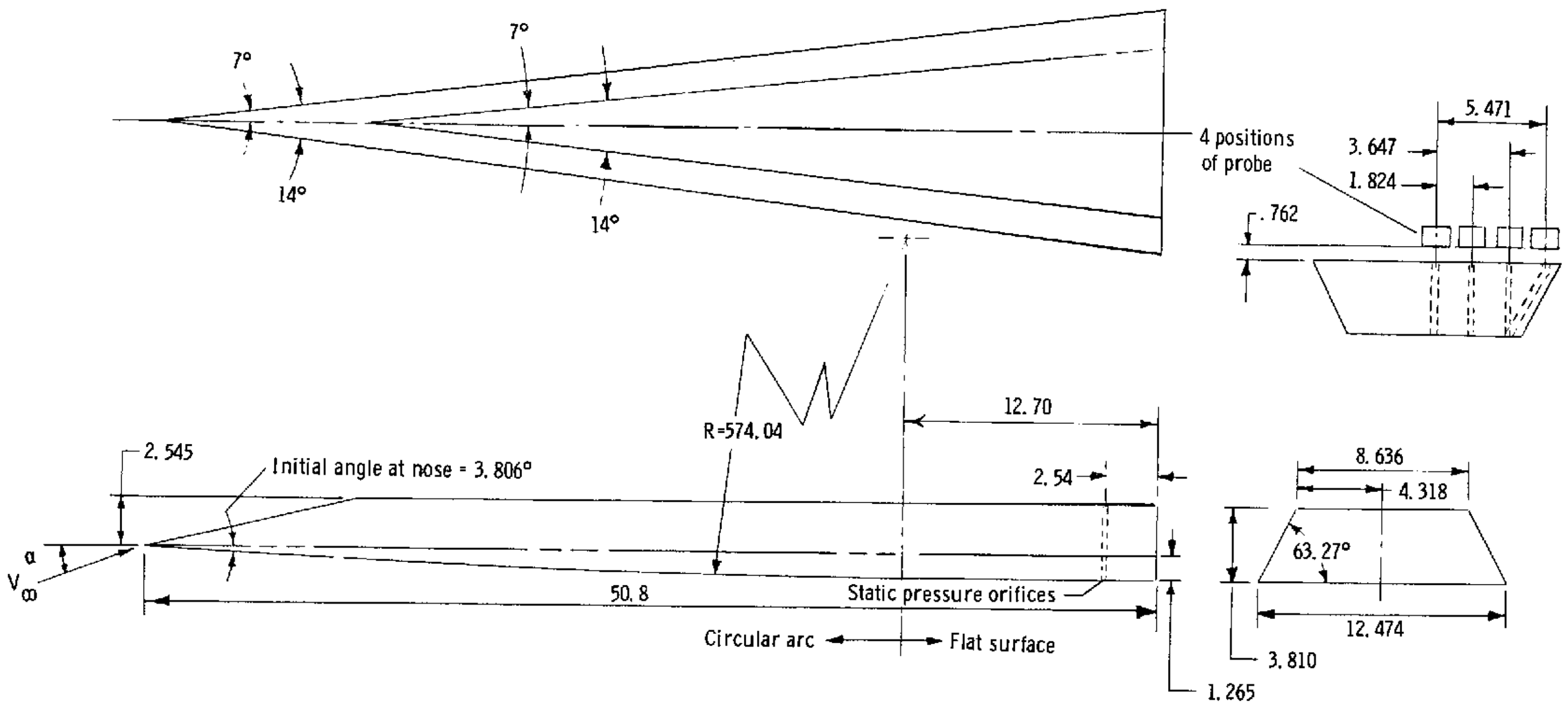

Figure 9.- Model number 7 – longitudinal-convex surface. All linear dimensions are in centimeters.

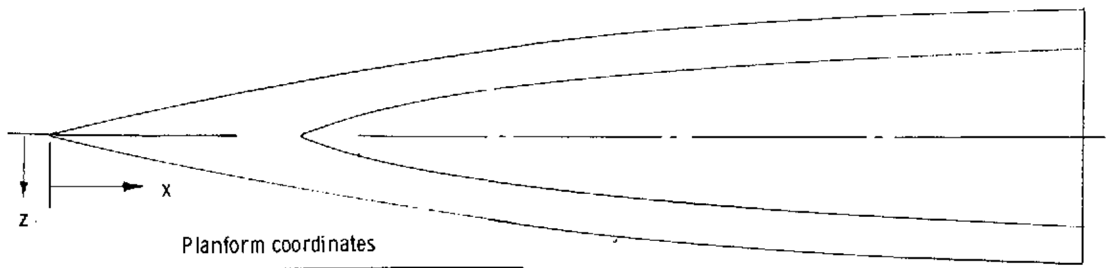

Planform coordinates

x	z	x	z	x	z
0	0	17.78	3.604	35.56	5.677
2.54	.610	20.32	3.993	38.10	5.847
5.08	1.186	22.86	4.353	40.64	5.987
7.62	1.732	25.40	4.679	43.18	6.096
10.16	2.248	27.94	4.976	45.72	6.175
12.70	2.731	30.48	5.240	48.26	6.220
15.24	3.183	33.02	5.474	50.80	6.237

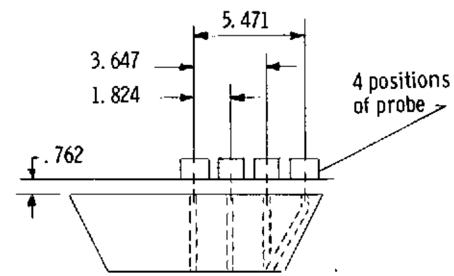

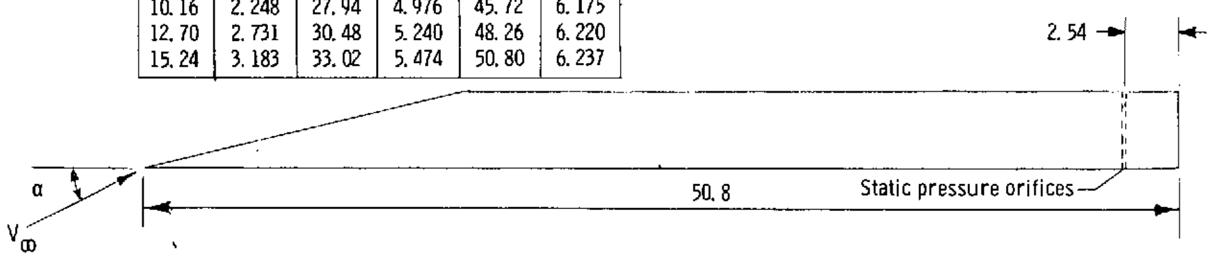

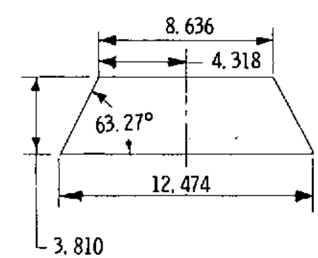

Figure 10.- Model number 8 – elliptical planform. All linear dimensions are in centimeters.

Lower surface coordinates at base

z	y	z	y	z	y
0	3.757	2.032	3.630	4.064	3.200
.254	3.754	2.286	3.592	4.318	3.124
.508	3.749	2.540	3.551	4.572	3.043
.762	3.739	2.794	3.505	4.826	2.957
1.016	3.726	3.048	3.454	5.080	2.865
1.270	3.708	3.302	3.398	5.334	2.769
1.524	3.683	3.556	3.338	5.588	2.667
1.778	3.658	3.810	3.271	5.710	2.616

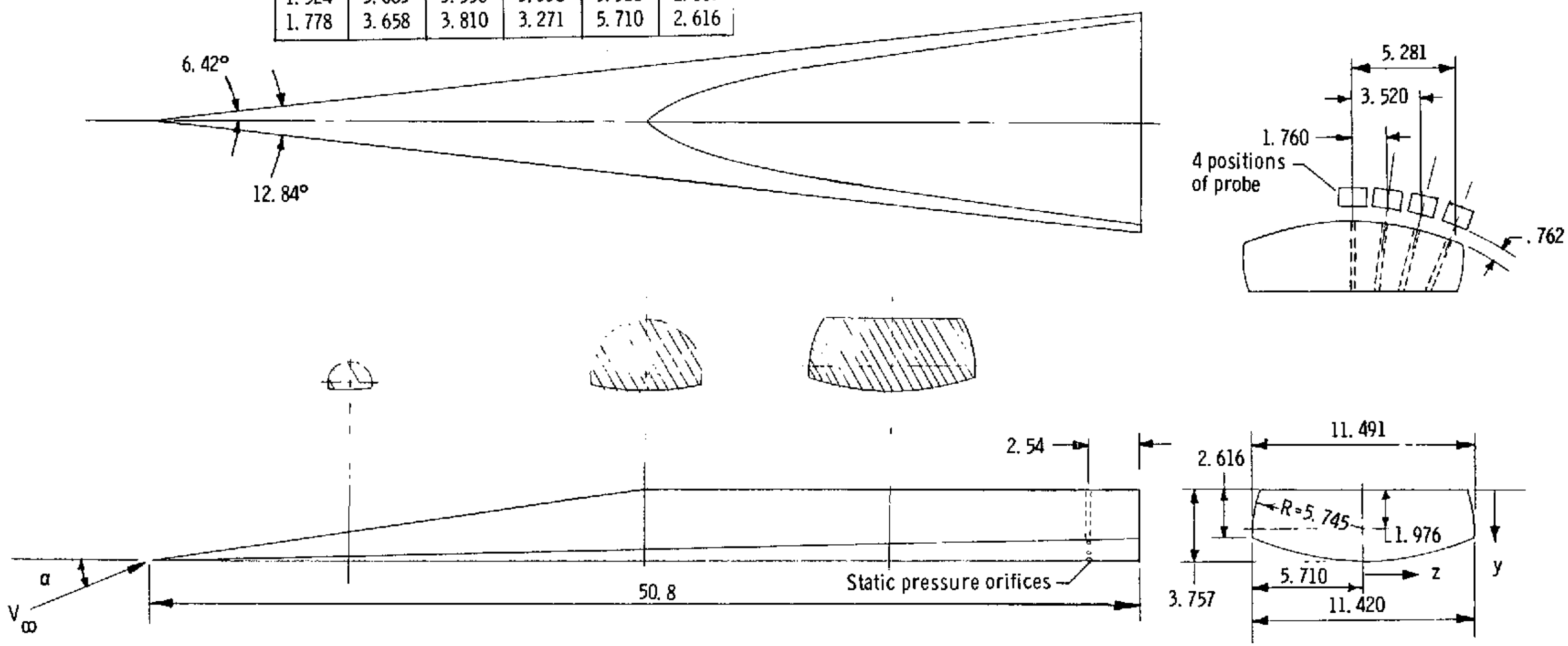

Figure 11.- Model number 9. All linear dimensions are in centimeters.

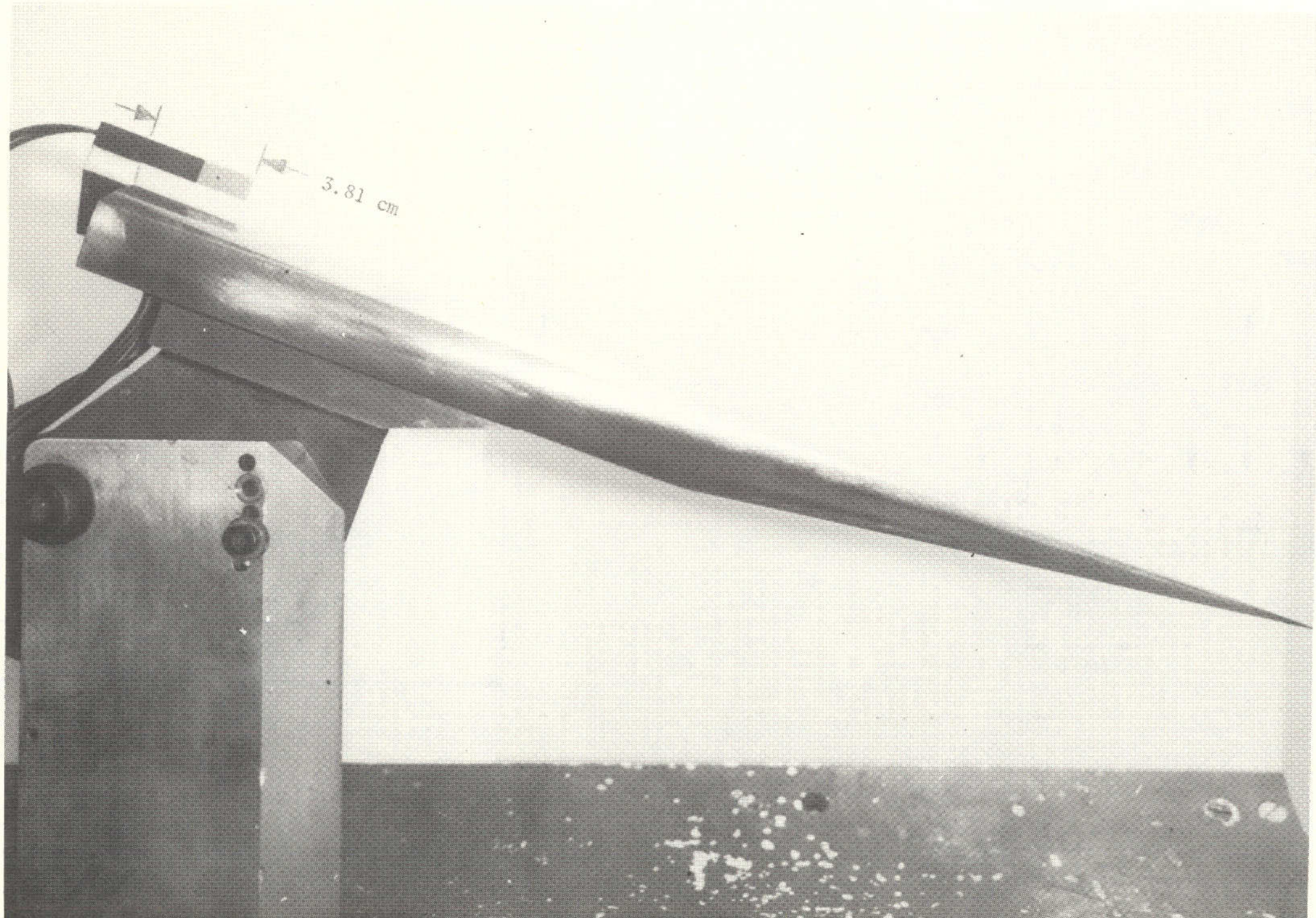

L-73-8814

Figure 12.- Photograph of forebody model number 9 with the flow-angularity probe mounted on the base.

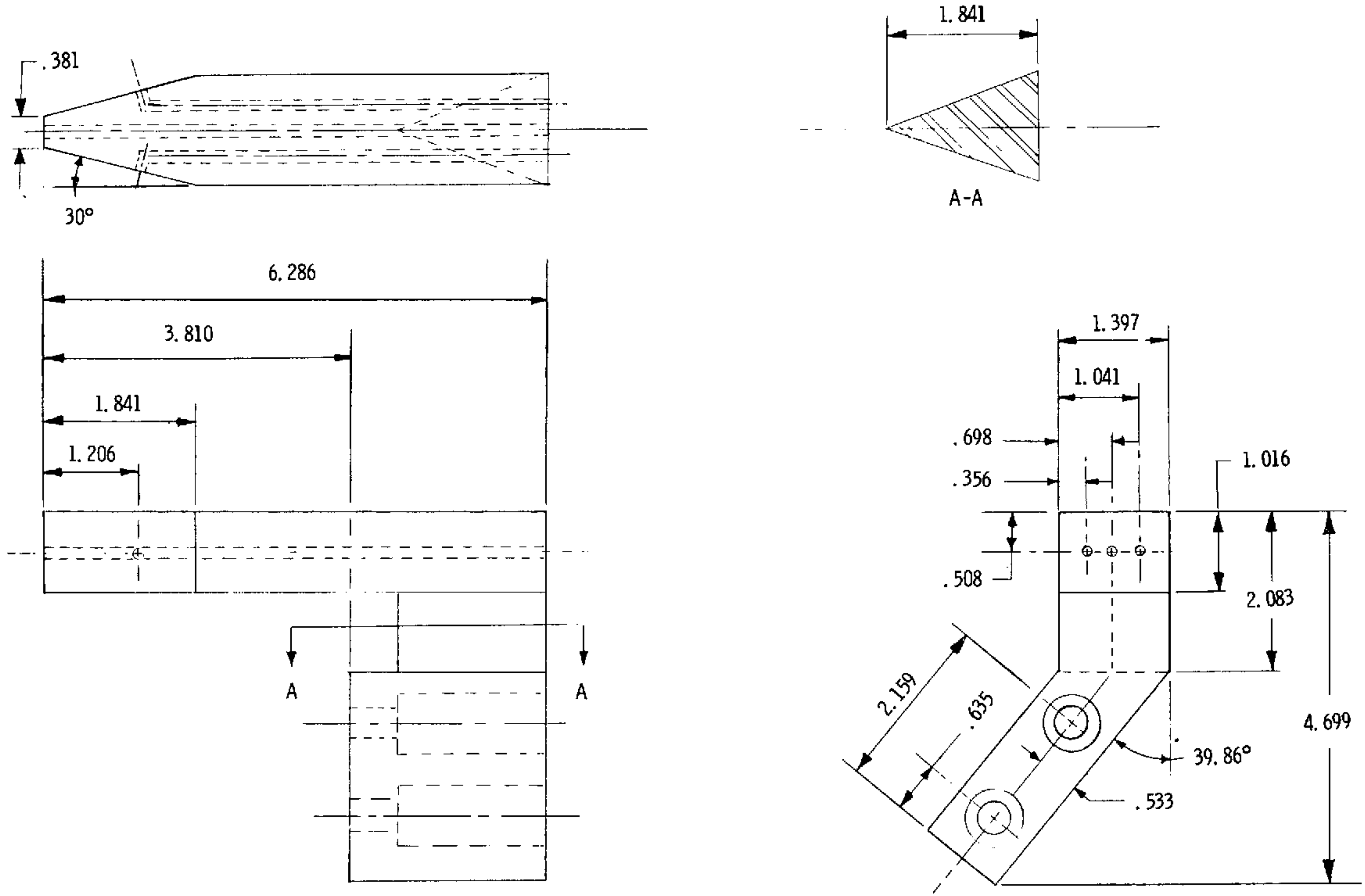

Figure 13.- Flow-angularity probe. All linear dimensions are in centimeters.

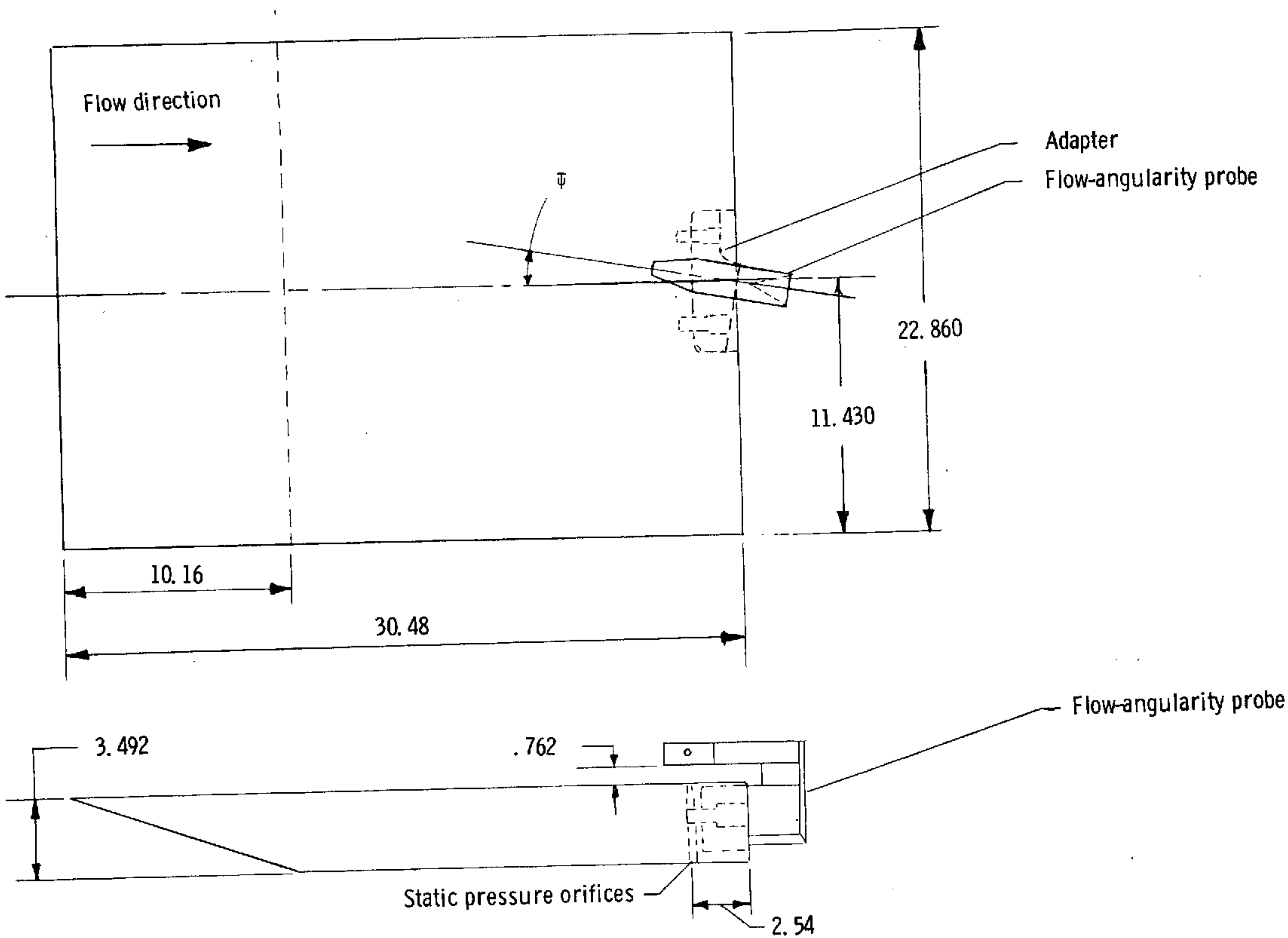

Figure 14.- Calibration plate for flow-angularity probe. All dimensions are in centimeters.

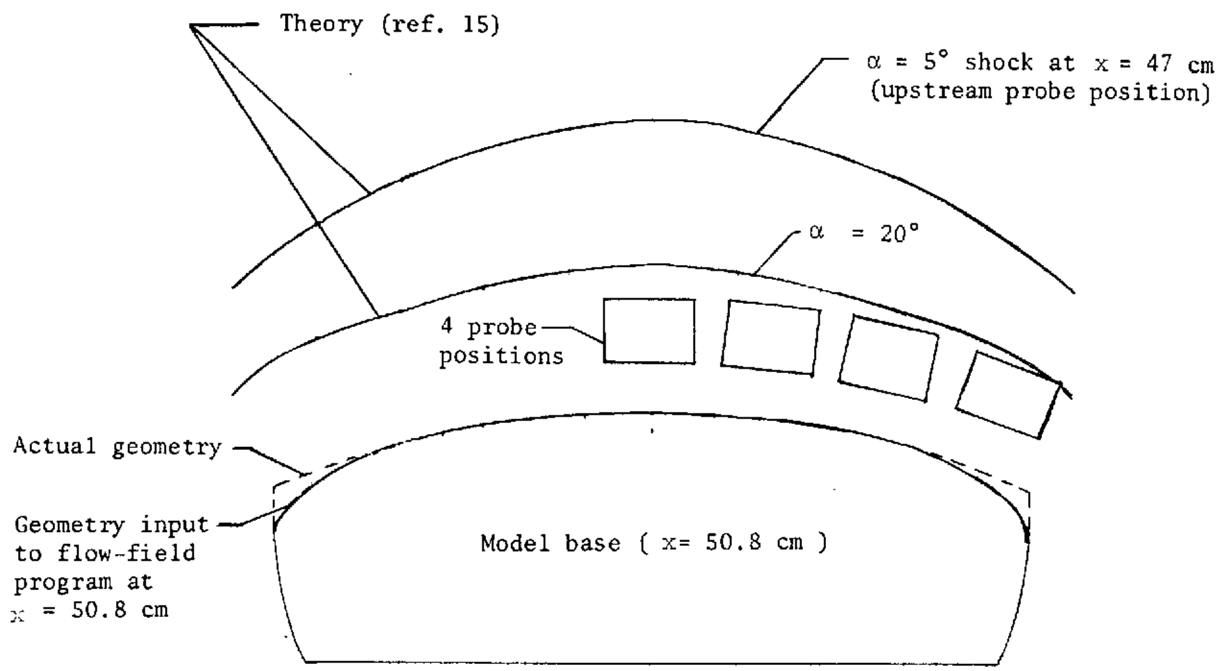

Figure 15.- Theoretical shock shapes for model 9 at leading edge of the probe (x = 47 cm).

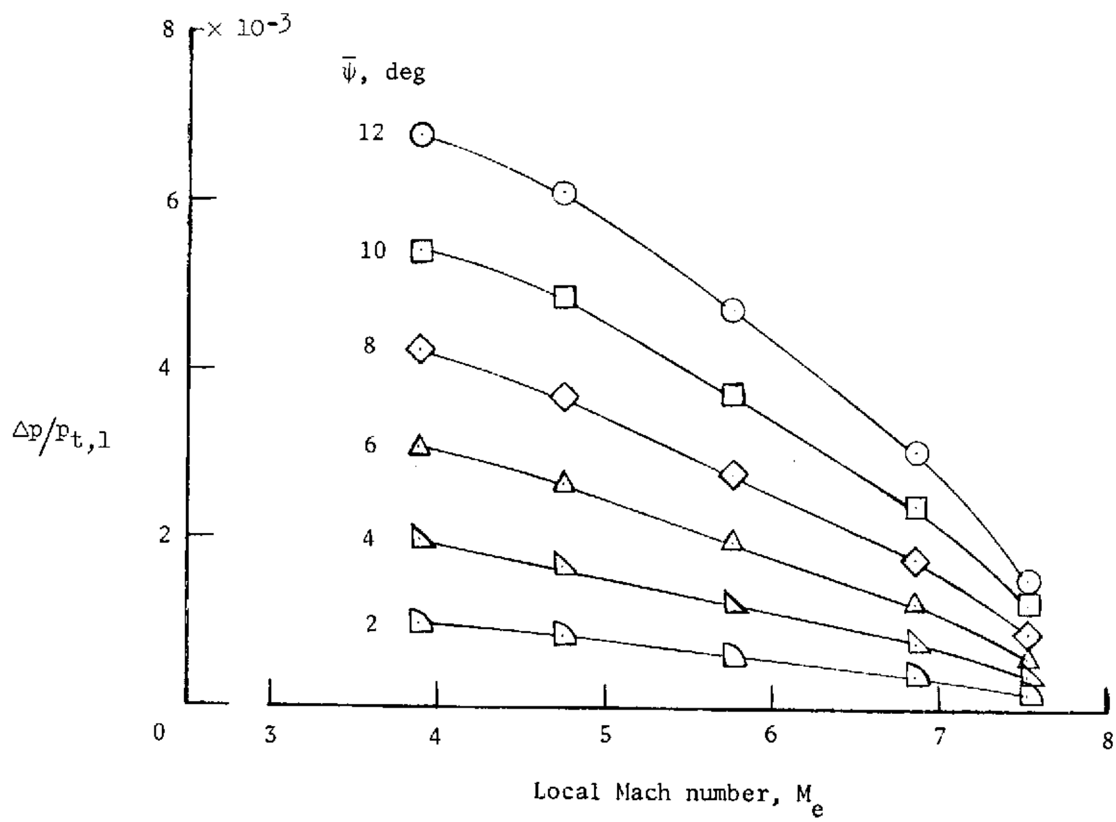

Figure 16.- Flow-angularity-probe calibration.

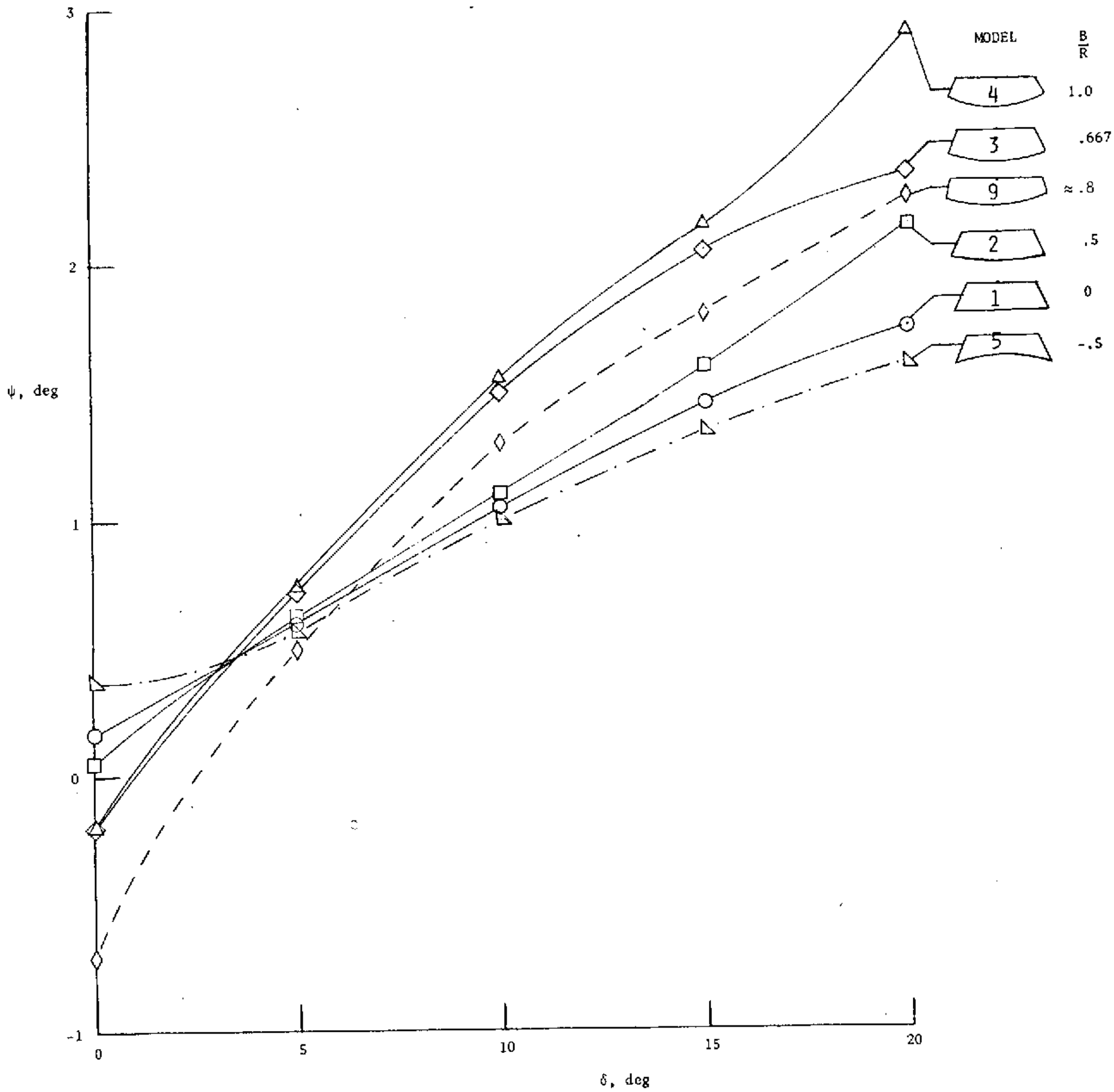

(a) 30 percent semispan station.

Figure 17.- Effect of spanwise curvature on flow angularity.

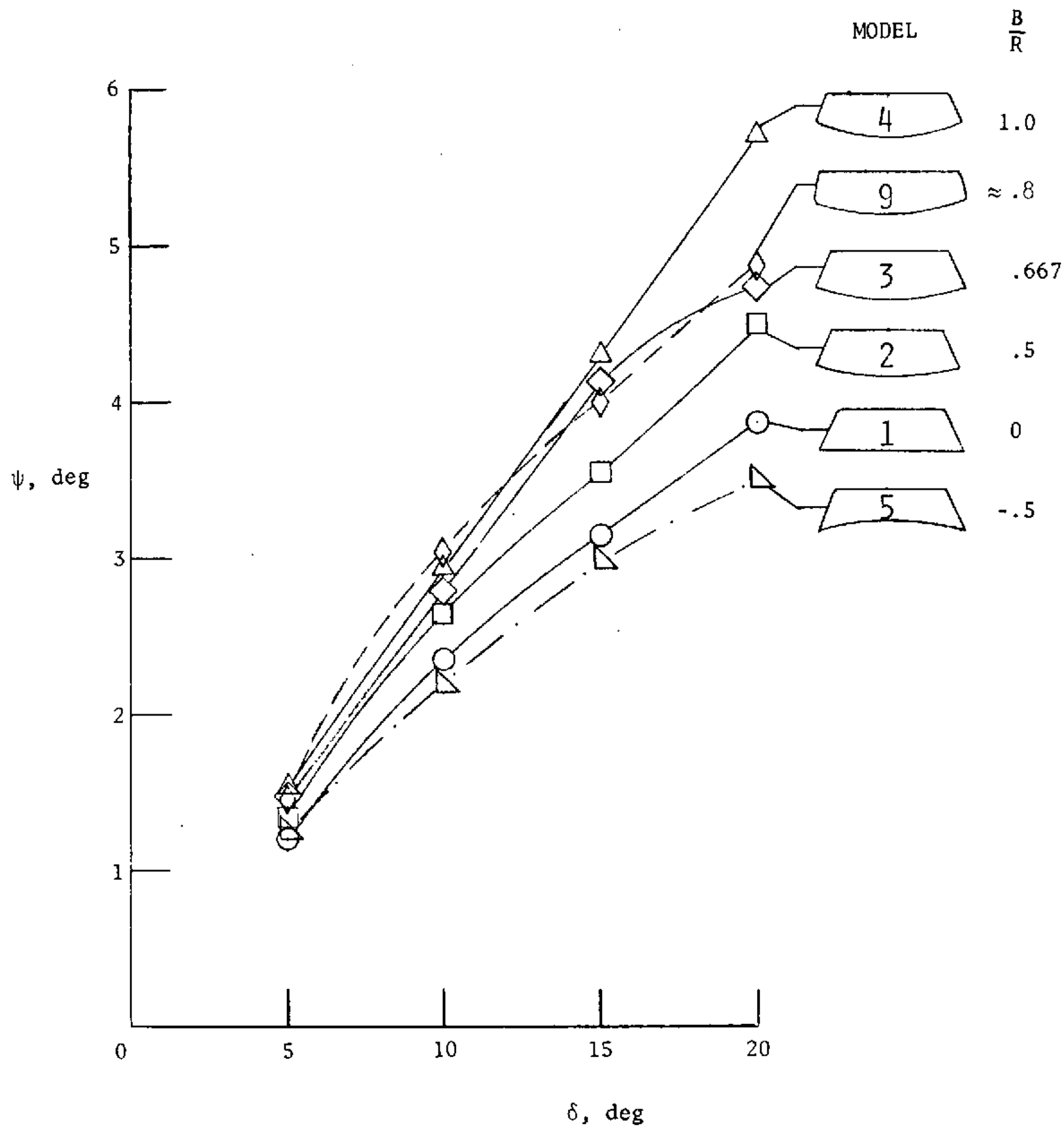

(b) 60 percent semispan station.

Figure 17.- Continued.

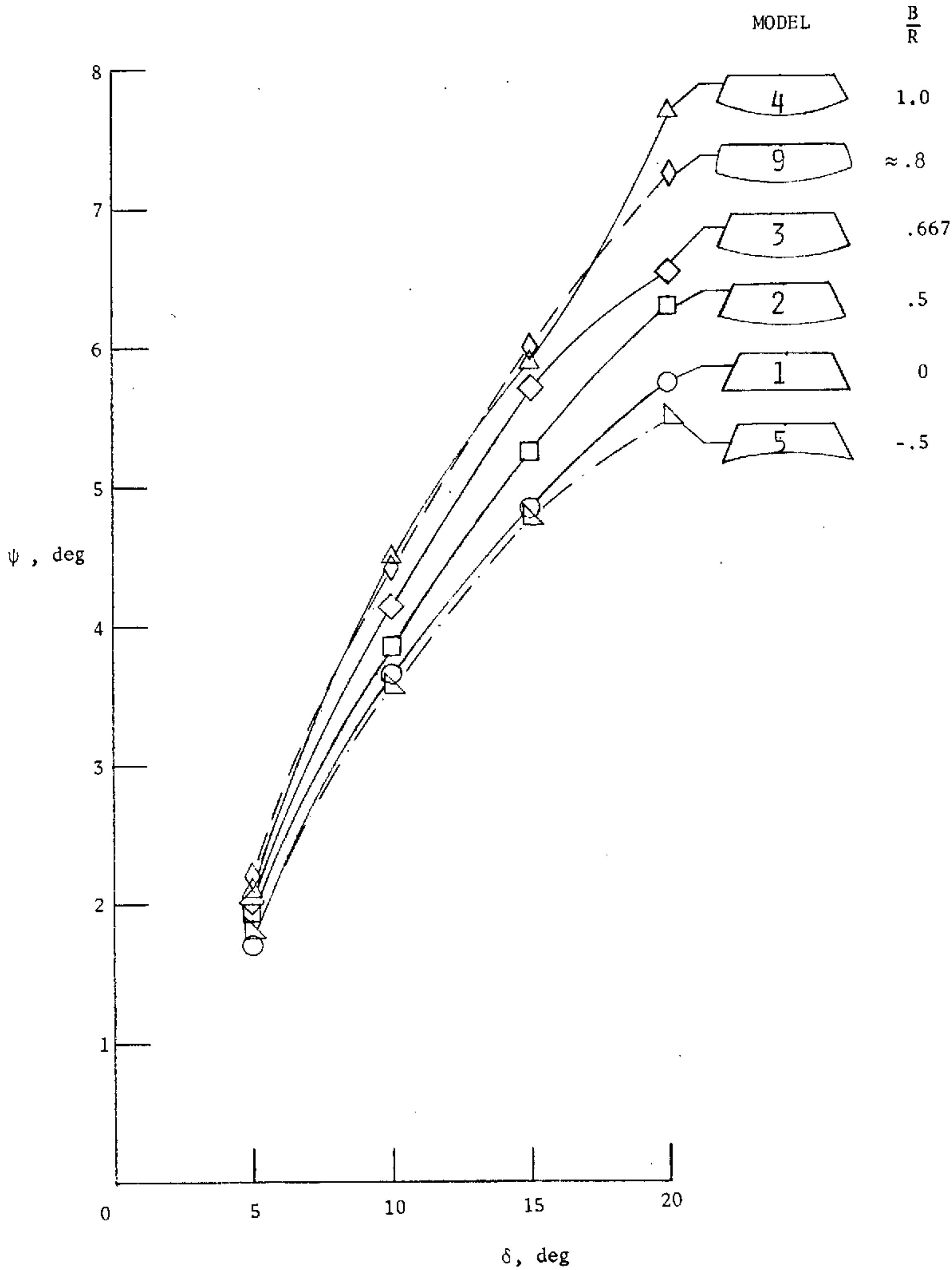

(c) 80 percent semispan station.

Figure 17.- Concluded.

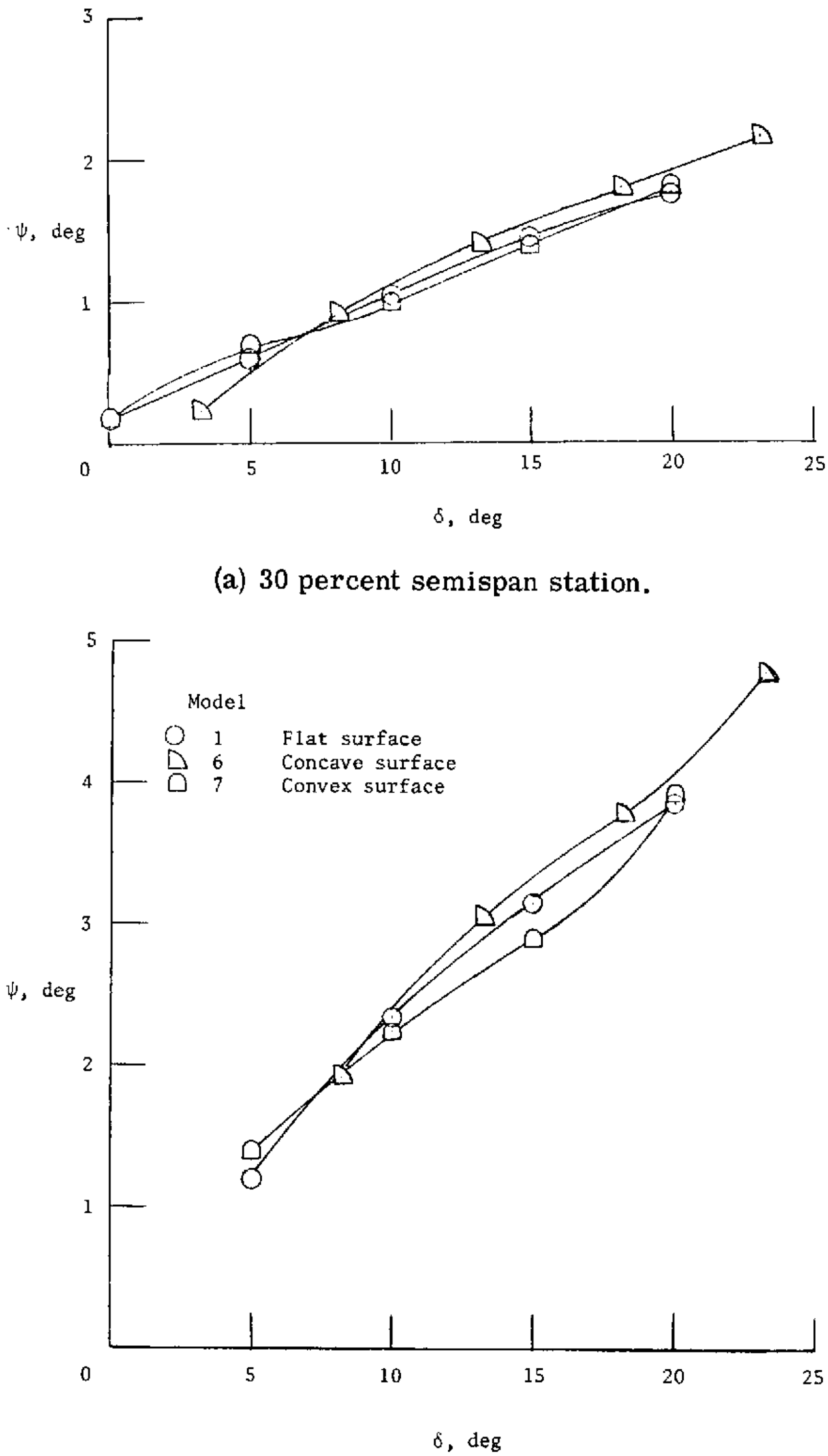

(a) 30 percent semispan station.

(b) 60 percent semispan station.

Figure 18.- The effect of longitudinal convex curvature (expansion) and longitudinal concave curvature (compression) on flow angularity.

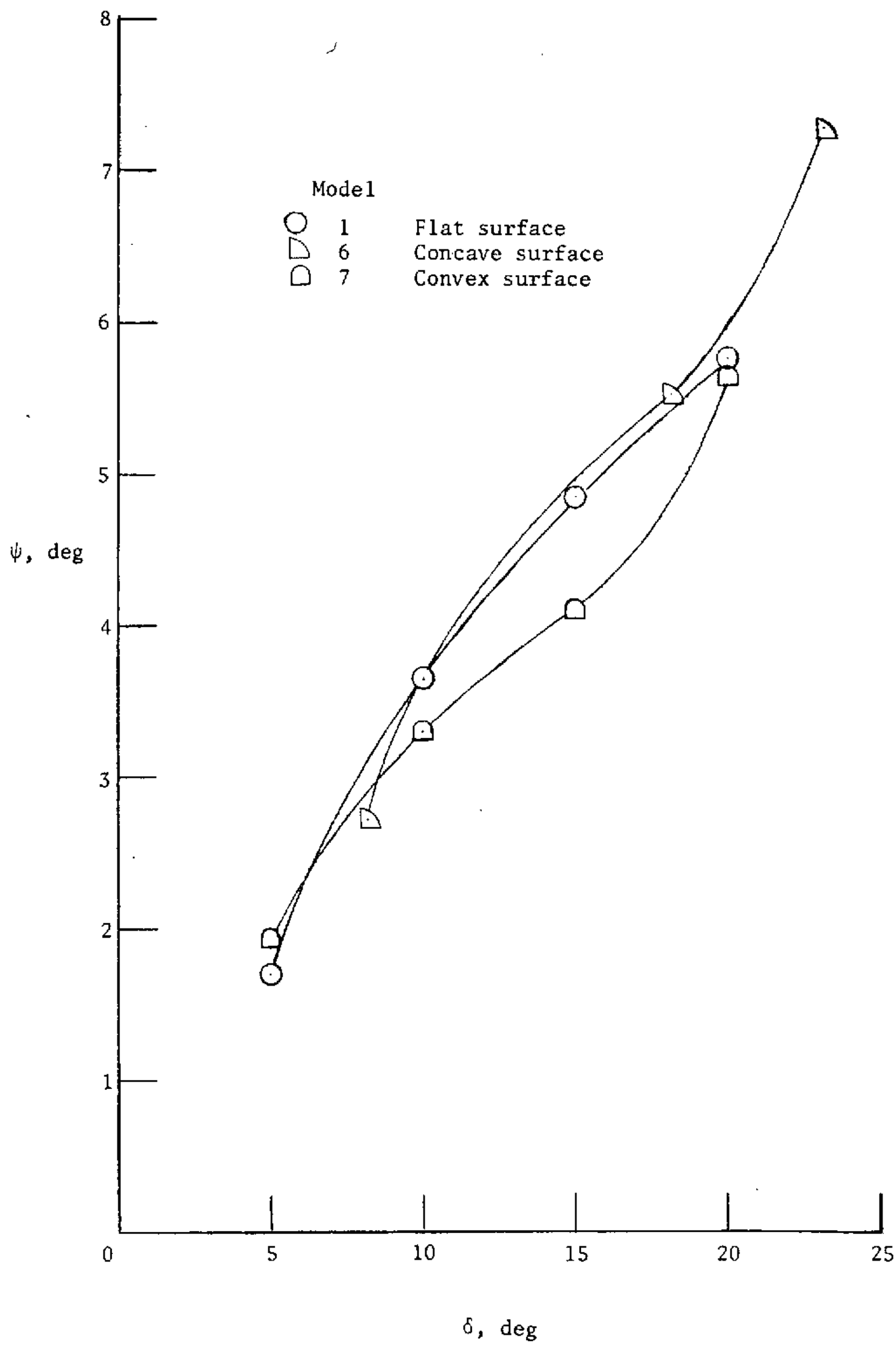

(c) 80 percent semispan station.

Figure 18.- Concluded.

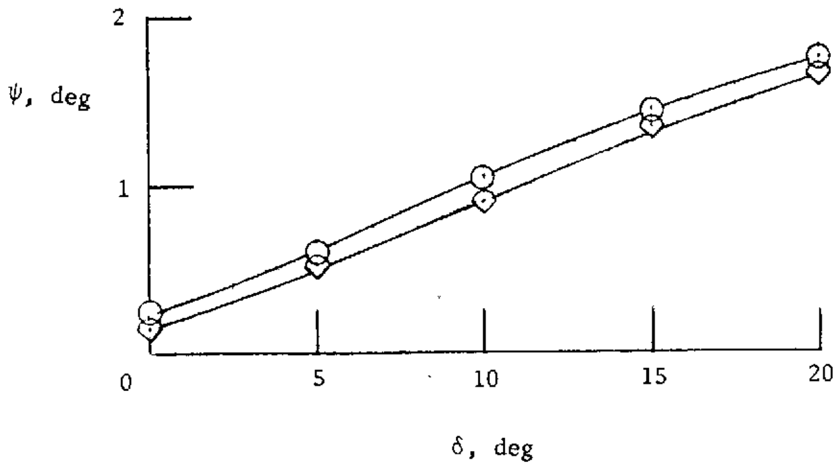

(a) 30 percent semispan station.

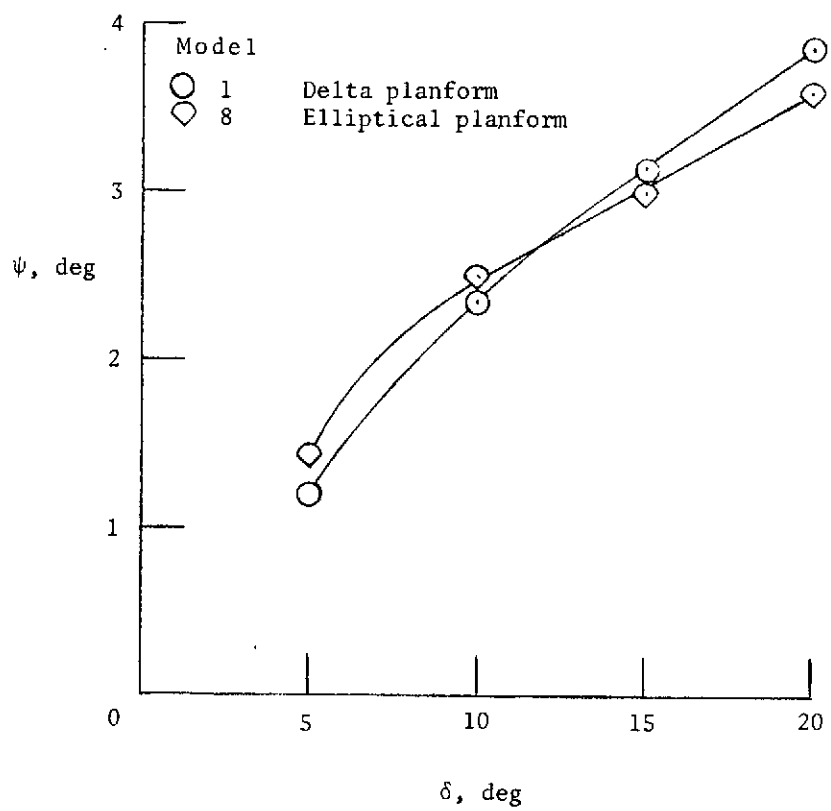

(b) 60 percent semispan station.

Figure 19.- The effect of planform change on flow angularity.

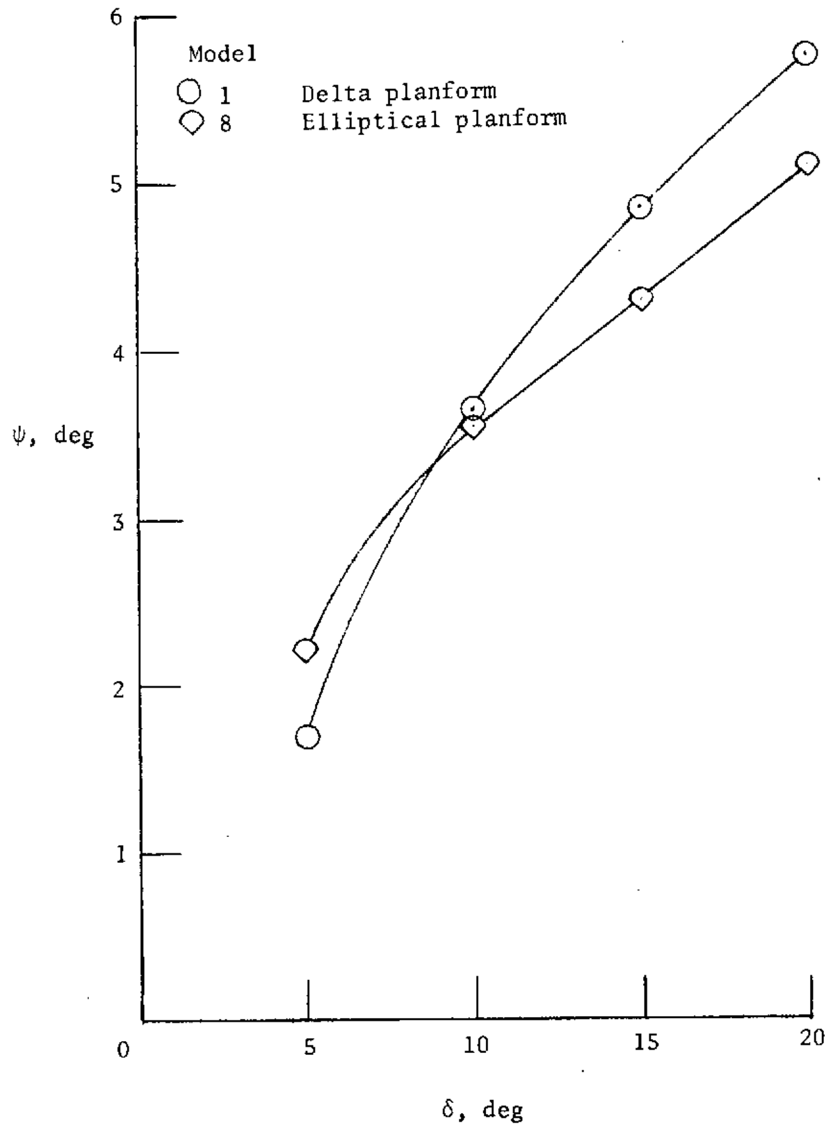

(c) 80 percent semispan station.

Figure 19.- Concluded.

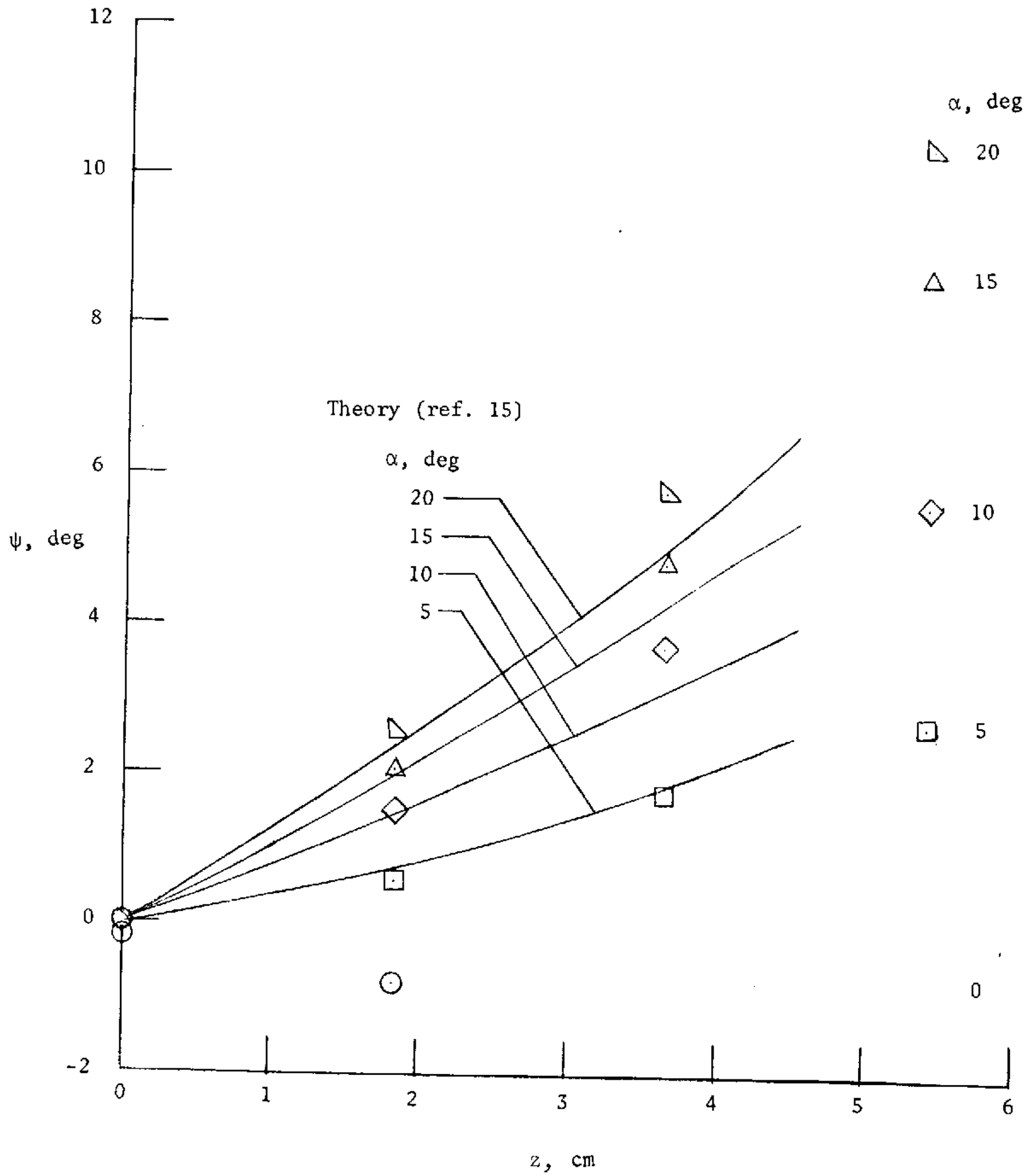

Figure 20.- A comparison of theoretical and experimental values of flow angularity for model 9 (z_{max} = 5.710 cm).

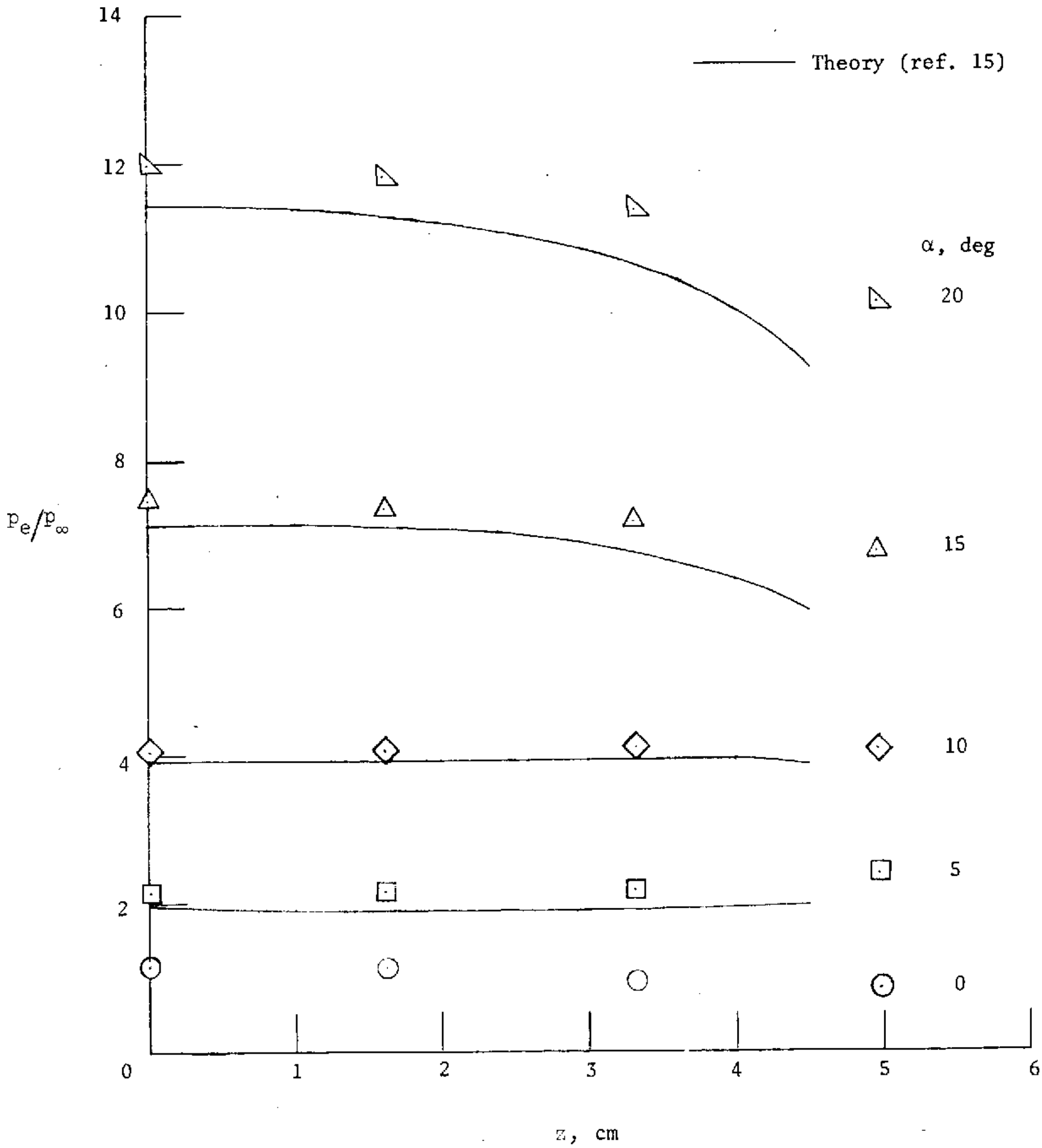

Figure 21.- A comparison of theoretical and experimental pressure distributions for model 9 (z_{max} = 5.710 cm).

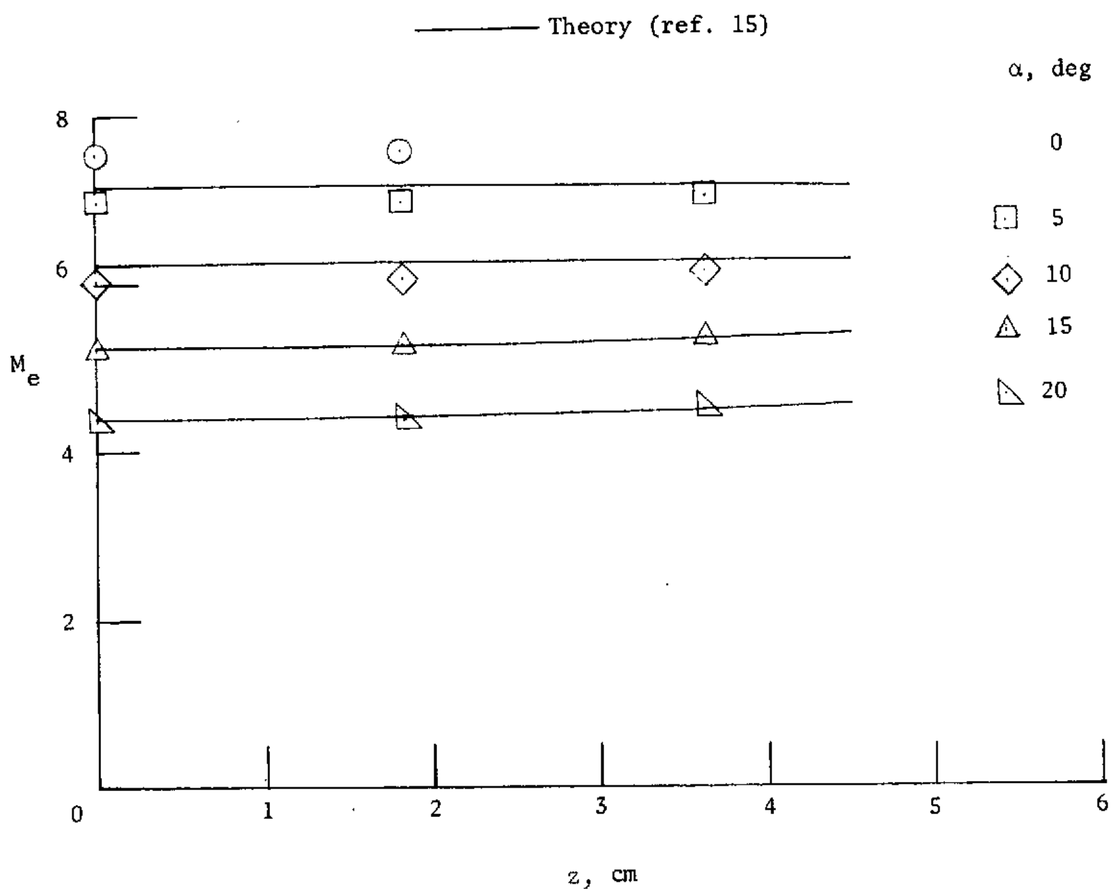

Figure 22.- A comparison of the local Mach number evaluated at the flow-angularity probe for model 9 (z_{max} = 5.710 cm).

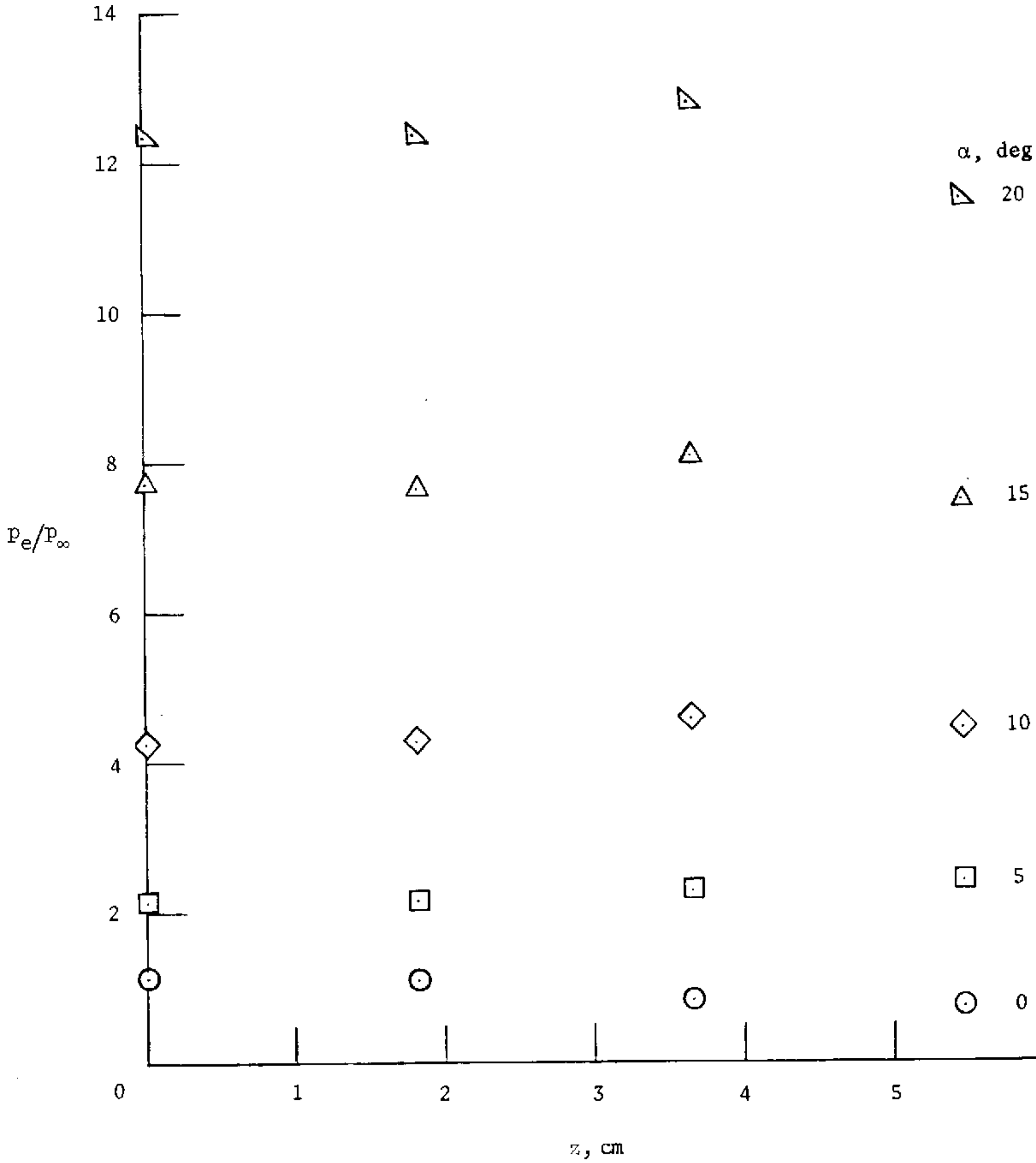

(a) Model 1 – flat-delta planform (B/R = 0; z_{max} = 6.237 cm).

Figure 23.- The effect of angle of attack on spanwise static pressure distributions.

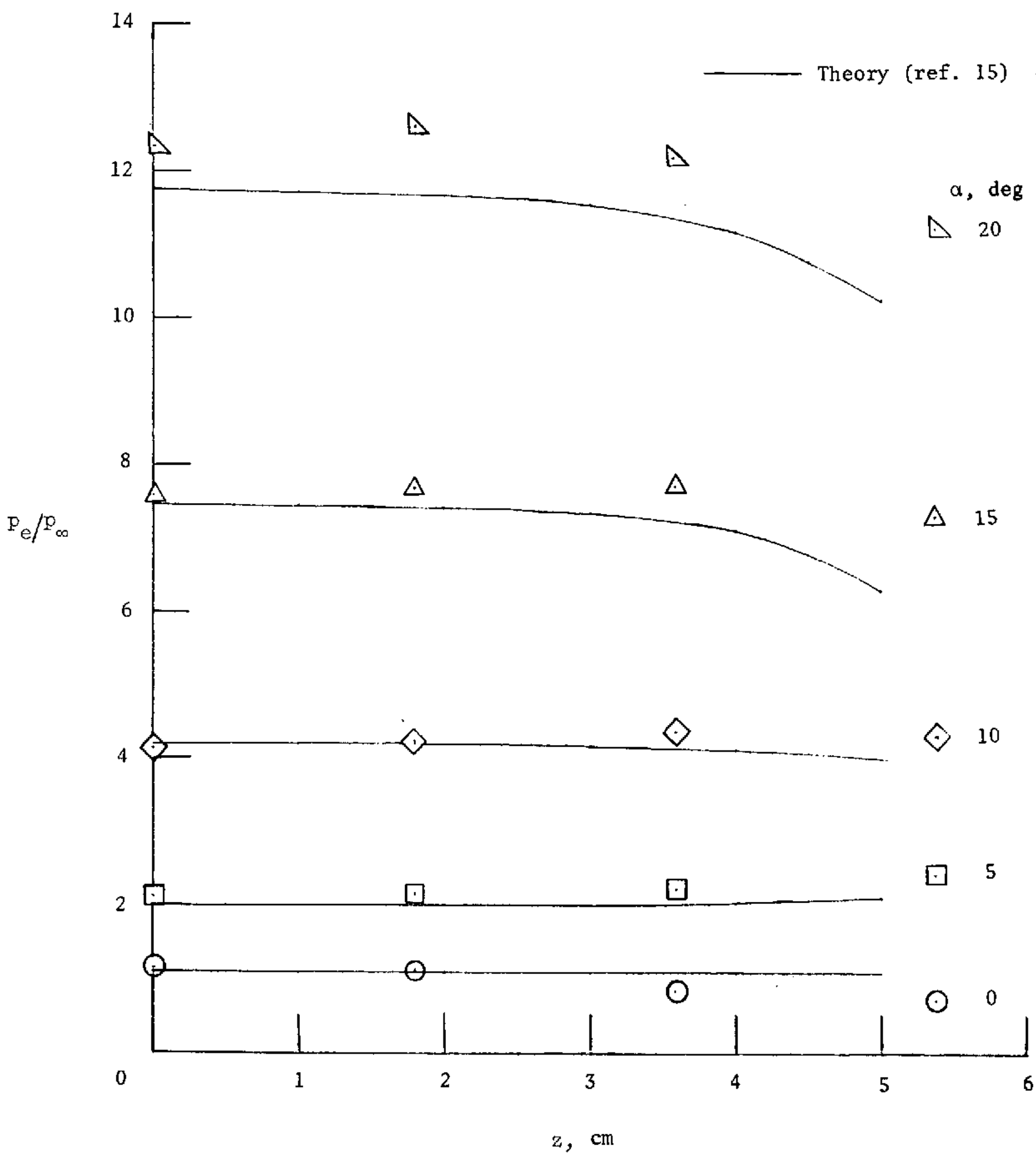

(b) Model 2 – spanwise-convex surface (B/R = 0.5; z_{max} = 6.237 cm).

Figure 23.- Continued.

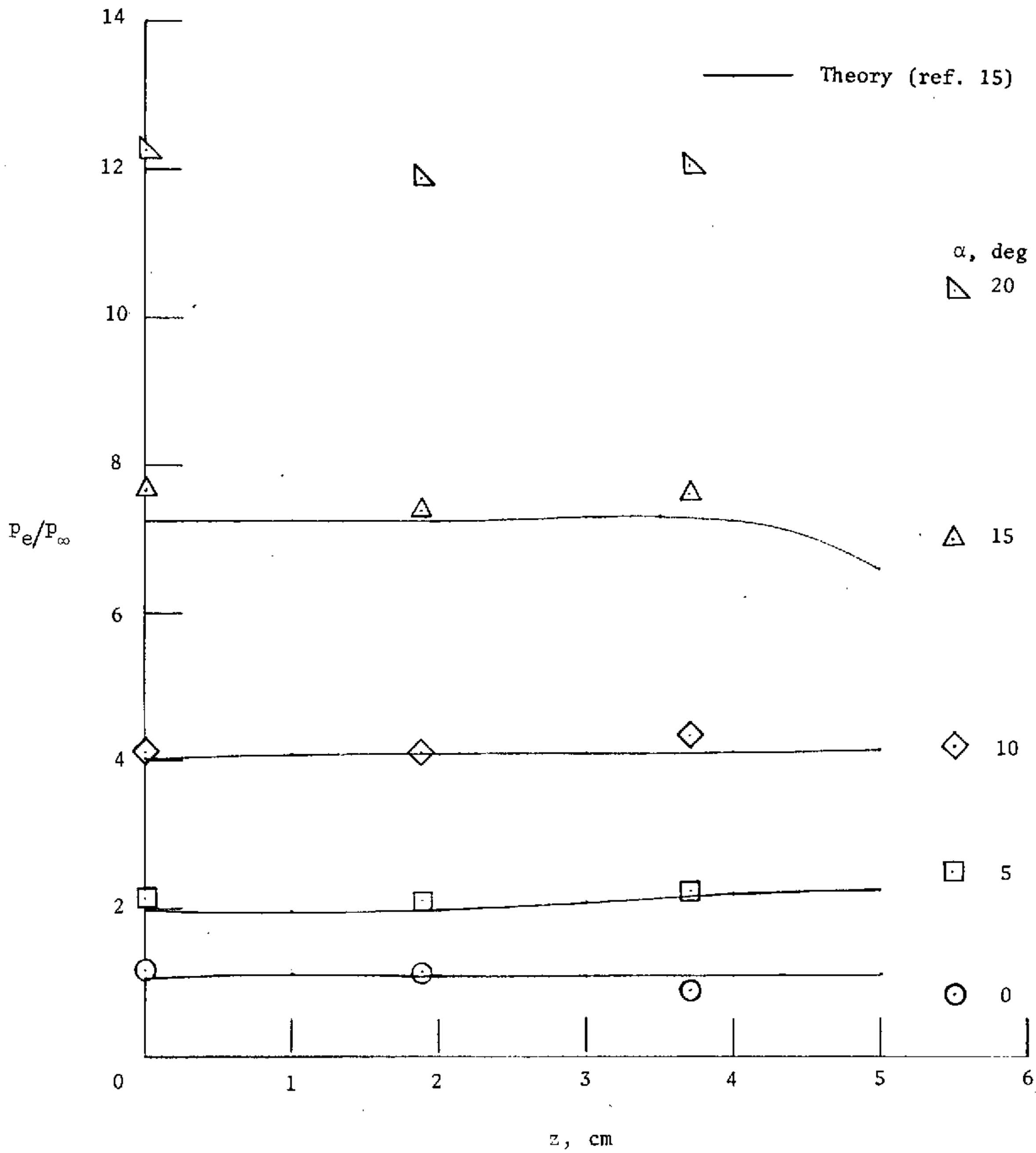

(c) Model 3 – spanwise-convex surface (B/R = 0.667; z_{max} = 6.237 cm).

Figure 23.- Continued.

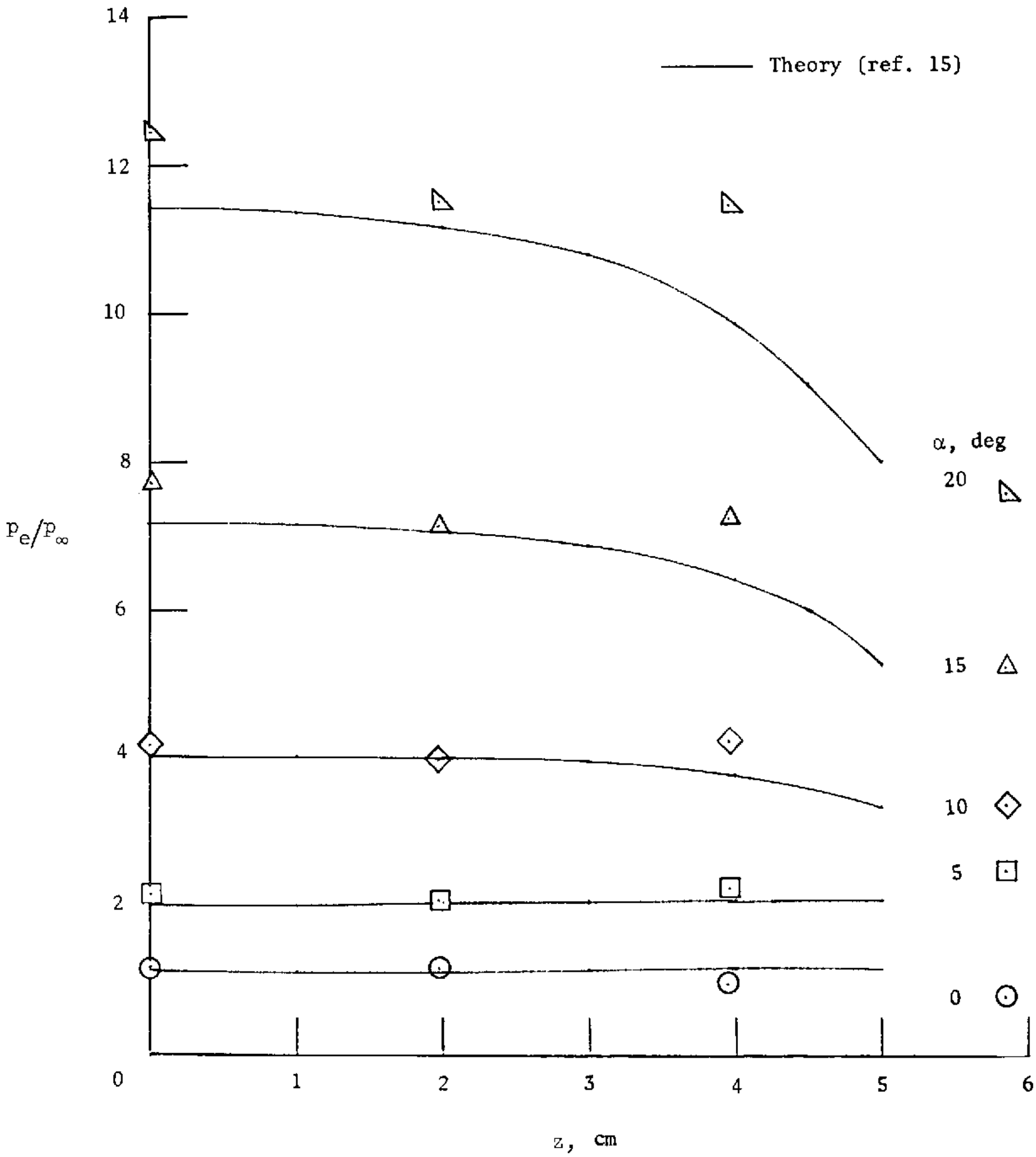

(d) Model 4 – spanwise-convex surface (B/R = 1.0; z_{max} = 6.237 cm).

Figure 23.- Continued.

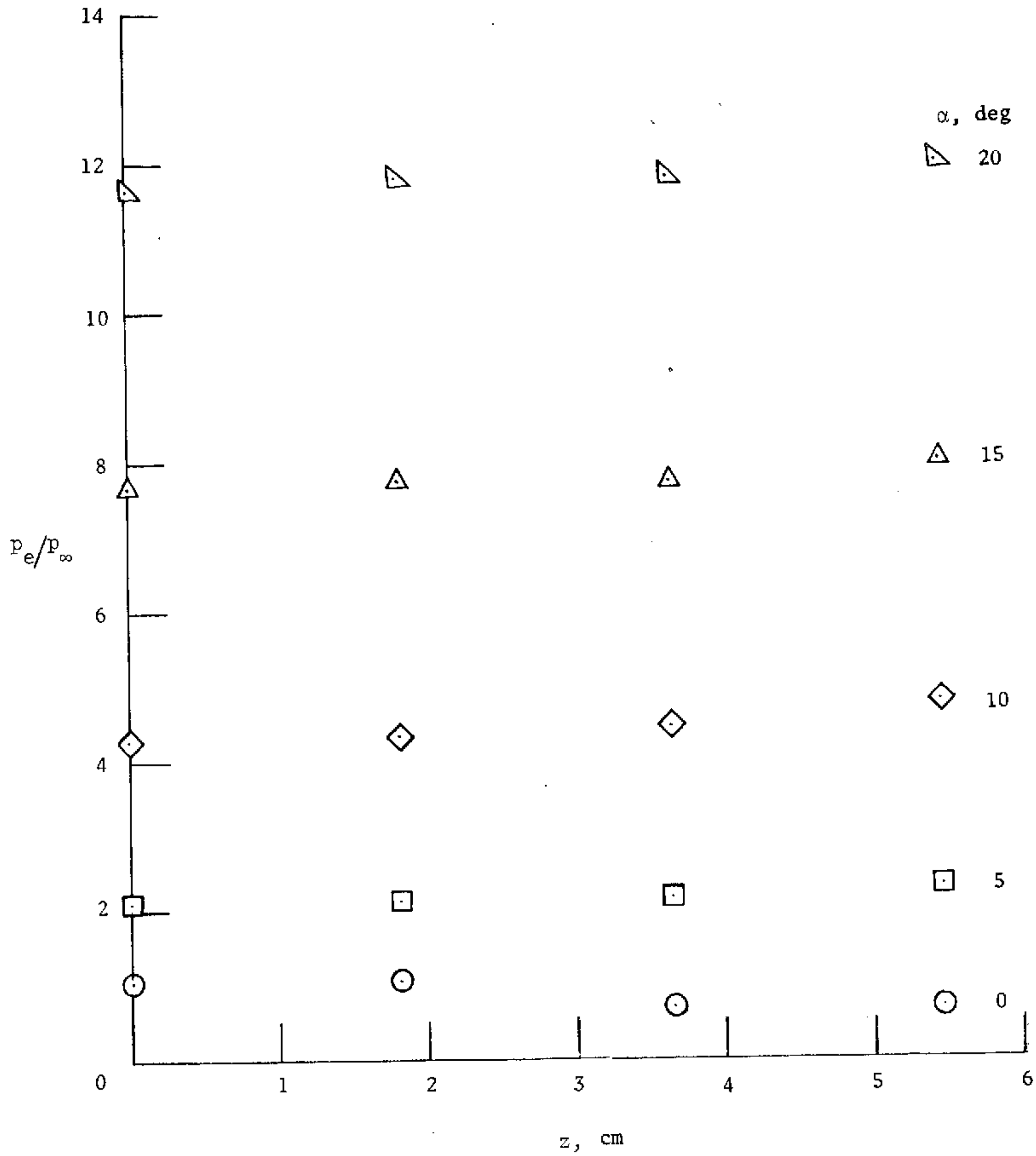

(e) Model 5 – spanwise-concave surface $\left(B/R = -0.5;\ z_{max} = 6.237\ \text{cm}\right)$.

Figure 23.- Continued.

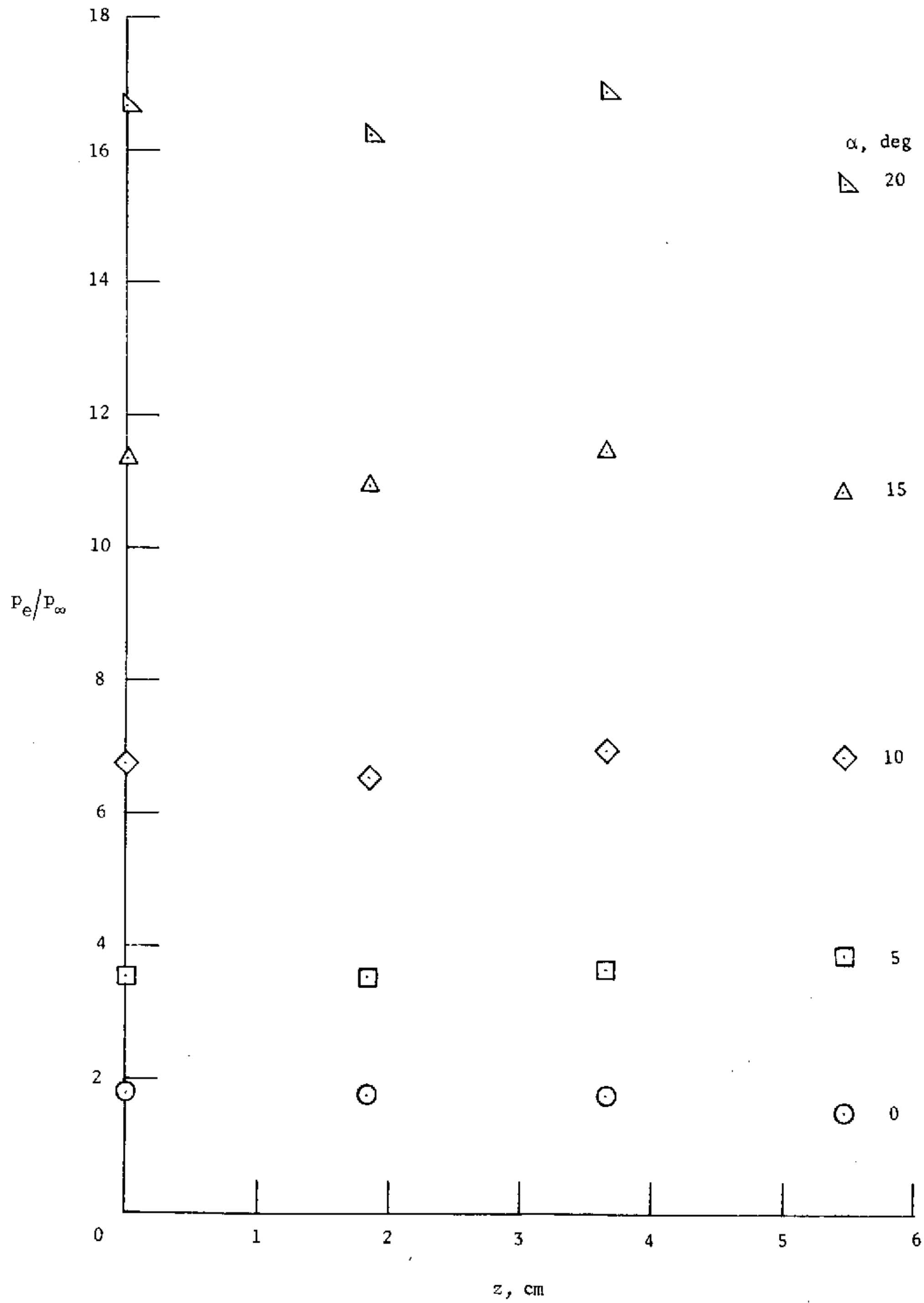

(f) Model 6 – longitudinal-concave surface (z_{max} = 6.237 cm).

Figure 23.- Continued.

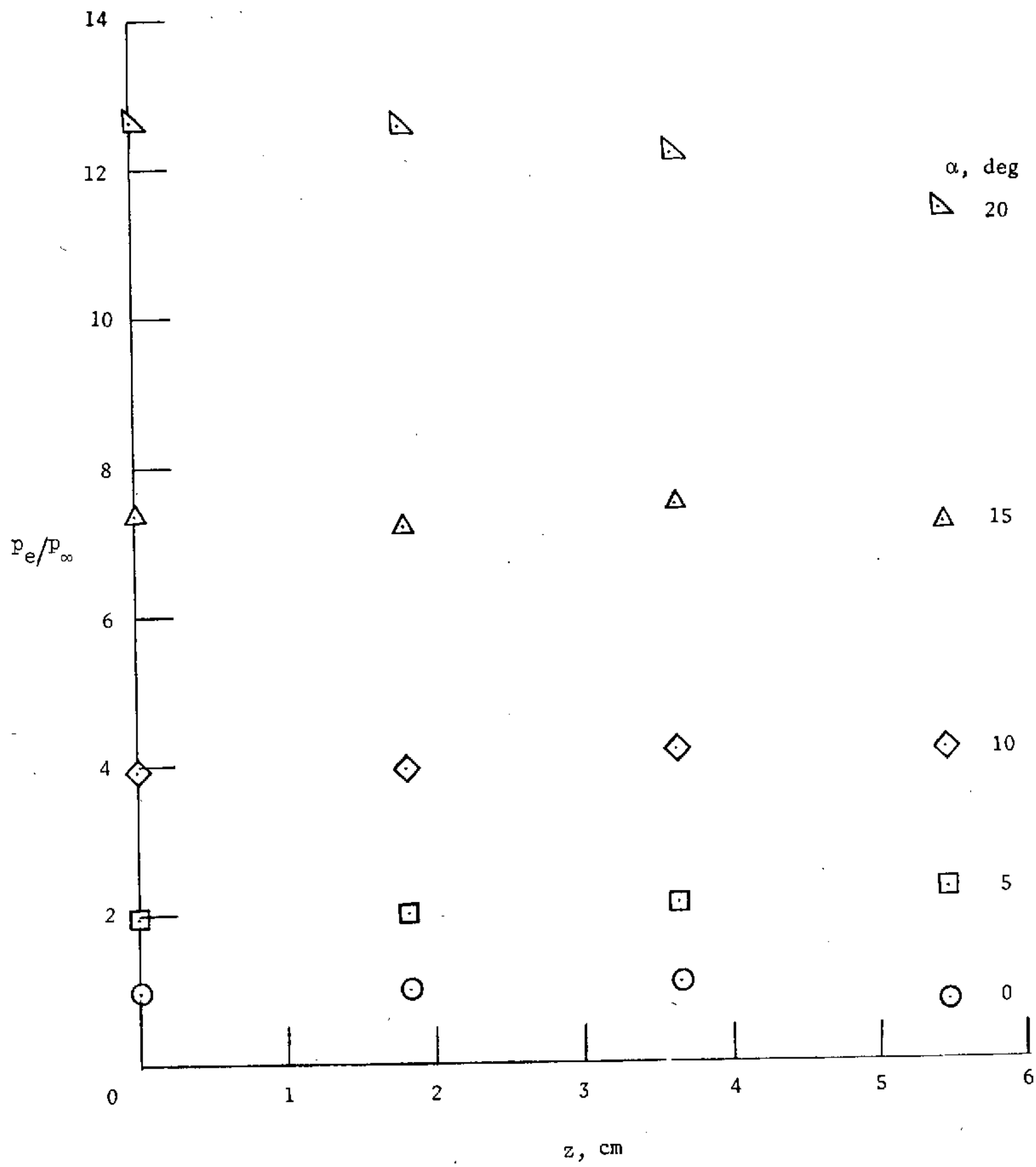

(g) Model 7 – longitudinal-convex surface (z_{max} = 6.237 cm).

Figure 23.- Continued.

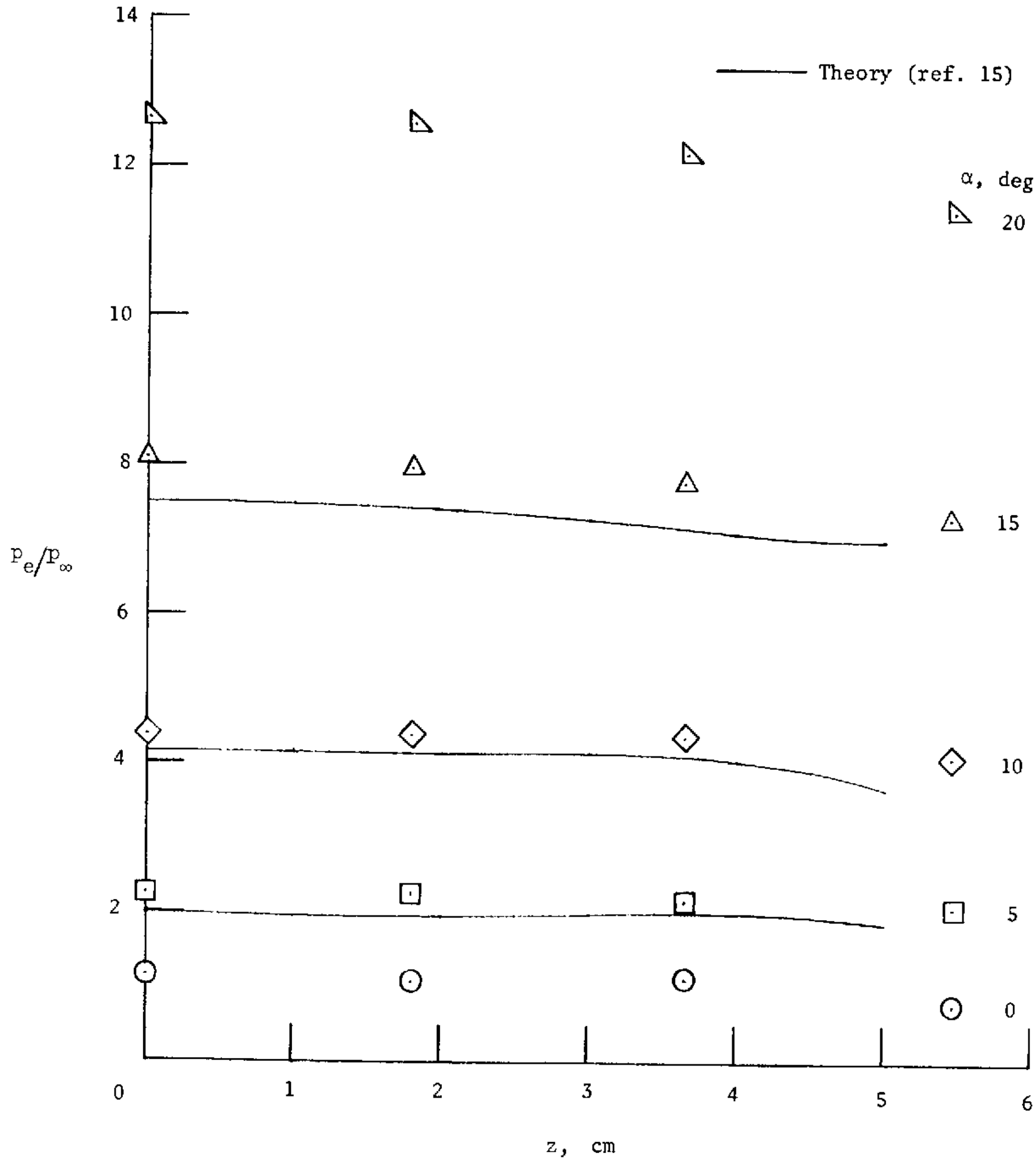

(h) Model 8 – elliptical planform (z_{max} = 6.237 cm).

Figure 23.- Concluded.

NASA-Langley, 1974 L-9639